Marine Structures 72 (2020) 102763

Contents lists available at ScienceDirect

Marine Structures

journal homepage: http://www.elsevier.com/locate/marstruc

Inhomogeneous wave load effects on a long, straight and side-anchored floating pontoon bridge

Jian Dai [a,*], Bernt Johan Leira [a], Torgeir Moan [a], Marit Irene Kvittem [b]

[a] Department of Marine Technology, Norwegian University of Science and Technology, 7049 Trondheim, Norway
[b] SINTEF Ocean, 7052 Trondheim, Norway

ARTICLE INFO

Keywords:
Floating bridge
Hydroelastic analysis
Inhomogeneous wave
Short-crested
Wind waves
Swell

ABSTRACT

In this paper, we present a numerical study on the hydroelastic response of a 4.6 km long fjord crossing floating bridge subjected to wave loads. The bridge is straight in design and supported by 35 pontoons along its full length. To limit the response to horizontal loads, four clusters of deep water mooring lines are engaged to increase the transverse stiffness of the bridge. Owing to the very large span across the fjord, inhomogeneity in the wave field exists. This study examines the various effects of inhomogeneous wave loads on the dynamic responses of the floating bridge. These include the spatial variations of the wave direction, significant wave height and peak period as well as the coherence and correlation of waves along the entire length of the floating bridge. For the purpose of comparison, the dynamic bridge responses under homogeneous wave load cases are also studied. In addition, the effects of wave load components and short-crestedness are presented and discussed.

1. Introduction

Bridges are essential infrastructures in connecting islands and land parcels separated by a water body to boost economic and leisure activities. When water is very deep and/or the seabed is extremely soft at a location where a bridge is going to be built, conventional piers supporting the bridge become expensive or even impractical. Under these conditions, floating bridges may offer distinct advantages through the use of natural buoyancy to support the bridge deck. Thus, the design of floating bridges is often independent of seabed conditions. More importantly, if the bridge is to be demolished or relocated elsewhere, a floating bridge allows easier removal than its bottom-founded counterpart as it may be towed away by tugboats. Owing to the advantages over the bottom founded bridges, the aftermath of World War II has witnessed a remarkable growth in the construction of floating bridges. Examples of modern floating bridges include the Mulberry Harbors [1], the Hood Canal Bridge [2], the Bergsøysund Bridge [3], the Nordhordland Bridge [4] and the Yumemai Bridge [5]. At the same time, a number of research studies on floating bridges were carried out [6–12].

The coastline of Norway is broken by many wide and deep fjords, and travel by road along the coastline takes time as it involves ferry connections. With the goal of substantially reducing the travel time, the Norwegian Public Road Authority (NPRA) initiated the E39 coastal highway project to replace fjord crossing ferry connections with floating structures, for example floating bridges, for road connections. It should be highlighted that designing cost-effective fjord crossing floating bridges faces many challenges. For example, the Bjørnafjord has a width of up to 5 km. With such a large span, the bridge structure is inevitably flexible and thus the coupling

* Corresponding author.
E-mail address: jian.dai@ntnu.no (J. Dai).

https://doi.org/10.1016/j.marstruc.2020.102763
Received 15 October 2019; Received in revised form 14 January 2020; Accepted 14 March 2020
Available online 10 April 2020

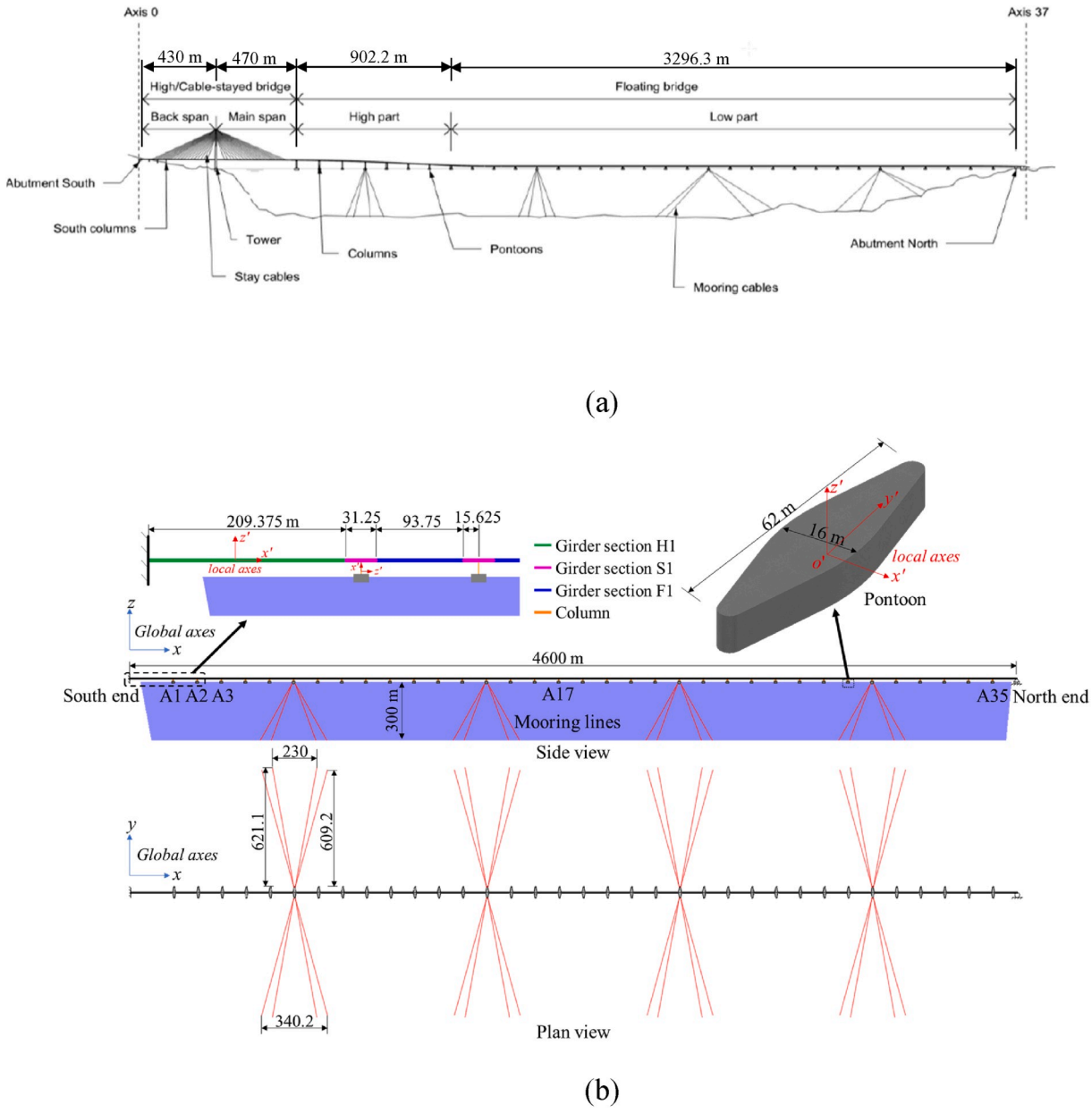

Fig. 1. Straight floating bridge: (a) design concept and (b) idealised model.

between the structural deformation and wave motion, i.e. the hydroelastic response of the floating bridge, becomes significant. Furthermore, the wave conditions across the fjord are found to be inhomogeneous [13]. This brings complications when it comes to the detailed modelling and analysis of the floating bridge. Although the common practice in engineering design is to apply the worst wave condition to the entire bridge structure, such an assumption could lead to underestimated responses in certain cases [14]. It is therefore important to include the inhomogeneity of wave conditions when examining the bridge responses.

The E39 project has led to many research activities on different design concepts of a floating bridge across the Bjørnafjord. Among the conceptual designs, a curved and end-anchored floating bridge concept, which has the advantage of avoiding mooring systems, attracts great research interests and many studies have been carried out. For example, the various wave load effects in a homogeneous condition on the curved floating bridge was examined by Cheng et al. [15]. The modelling of inhomogeneous wave loads and their effect on the floating bridge were presented by Cheng et al. [16]. Xu et al. [17,18] investigated the effect of hydrodynamical interaction between pontoons on the global responses of the curved floating bridge. The study revealed that the direction of wave heading influences the hydrodynamical coupling but the overall effect on the floating bridge is limited due to a large spacing between the pontoons. The effect of wave directionality on the extreme bridge responses was studied by Viuff et al. [19]. A code-to-code

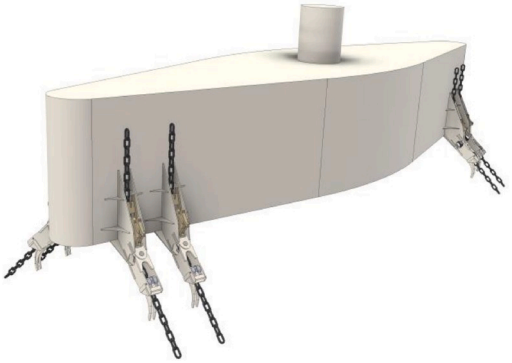

Fig. 2. Illustration of connection between mooring lines and pontoon [23].

comparison of the dynamic characteristics of the curved floating bridge was also carried out by Viuff et al. [20] using commonly applied commercial solvers. In addition, the effect of ship collision into pontoons and bridge girders were investigated by Sha et al. [21, 22].

It is no doubt that curved structures are effective in resisting transverse loads through the arch effect instead of the beam bending action. With a span near 5 km, however, the stiffness of the bridge in its curvature plane becomes quite low. Furthermore, the dynamic environmental loads and parametric resonance can result in large axial compression forces that may trigger buckling of the bridge structure. Without deep water mooring systems, the curved bridge also lacks hydrodynamic damping which is important in mitigating the dynamic bridge responses under environmental loads. As an alternative, a straight, side-anchored floating bridge may be a cost-effective solution. As a straight bridge does not rely on the membrane action to carry transverse loads, the restraint imposed on the axial deformation to mobilise the arch action for curved bridges does not apply. Consequently, axial elongation and contraction due to thermal effects are allowed which also reduce the risk of global buckling of the bridge girder. In addition, the provision of mooring lines can effectively increase the transverse stiffness of the bridge while adding viscous hydrodynamic damping to the bridge structure. Due to the distinct differences in the structural configurations, curved and straight bridges have very different vibration modes and natural periods from each other. Therefore, their dynamic responses are expected to be quite different even under the same environmental conditions. Knowing the dynamic behaviour of a long, straight and side-anchored floating bridge in an inhomogeneous wave environment is thus important and beneficial to both researchers and engineers in their studies of similar structures. However, such studies are rather limited in the open literature.

In this paper, we present a comprehensive numerical study on the hydroelastic responses of a 4.6 km long straight, side-anchored floating pontoon bridge subjected to wave loads. The vertical stiffness of the bridge is provided by 35 evenly spaced pontoons along the bridge girder. The transverse motion of the bridge is restrained by clusters of mooring lines tethered at four pontoons. Owing to the very large span and hydrology topology across the Bjørnafjord, inhomogeneity in the wave field exists. Various effects of inhomogeneous wave conditions on the hydroelastic responses of the floating bridge are also examined. These include the inhomogeneity in wave direction, significant wave height, peak period as well as the coherence and correlation of waves at different locations along the entire length of the floating bridge. For the purpose of comparison, the bridge responses under homogeneous wave load cases are also studied. In addition, the effects of wave load components and short-crestedness are presented and discussed.

The remainder of the paper is organised as follows. Section 2 defines the problem and describes the computational models and methodology for numerical implementation. Section 3 establishes the homogeneous and inhomogeneous wave load cases, followed by a comprehensive examination of the various wave load effects on the bridge responses presented in Section 4. Finally, Section 5 concludes the findings of the study.

2. Methodology and mathematical formulation

2.1. Problem definition

The conceptual design of a straight floating pontoon bridge across the Bjørnafjord is presented in Fig. 1(a) [23]. The bridge contains a cable-stayed bridge section at the south end for navigation purposes, a transitional high part and a low part which is the main floating bridge section with box girders 18 m above the water surface and supported by pontoons at a spacing around 125 m. Both the girders, columns and pontoons are made of structural steel. The transverse motion of the floating bridge is restrained by four clusters of deep water mooring lines spaced about 1 km apart along the length of the bridge.

In order to focus on the wave load effect on the floating bridge section, this study employs an idealised, generic floating bridge model based on the low part of the design concept. As illustrated in Fig. 1(b), the simplified floating bridge, 4.6 km long and 18 m elevated above the water surface, is resting on 35 evenly spaced pontoons (which are referred to by their location as A1 to A35) and held in position by four mooring clusters. The water depth is set to 300 m and assumed to be constant throughout the entire bridge length. In view of the overall dimensions of the bridge, the girders and columns are reasonably modelled as Euler-Bernoulli beams and

Table 1
Bridge girder and column sectional properties.

Section	Mass (kg/m)	Sectional area (m^2)	$I_{x'}$ (m^4)	$I_{y'}$ (m^4)	$I_{z'}$ (m^4)	$I_{x'x'}$ (kg/m·m^2)
Girder H1	17530	1.38	5.79	2.87	107.22	1.2×10^6
Girder S1	19780	1.65	7.88	4.06	116.52	1.3×10^6
Girder F1	16040	1.17	6.64	3.21	89.88	1.1×10^6
Column	9180	1.53	14.92	9.65	12.94	2.3×10^5

Table 2
Pontoon properties.

Type	Freeboard (m)	Draft (m)	Mass (ton)	Planar area (m^2)	Radius of gyration		
					$r_{x'}$ (m)	$r_{y'}$ (m)	$r_{z'}$ (m)
Unmoored	3.5	5.0	850	667	16.1	5.2	16.3
Moored	3.5	8.5	1452	667	17.0	6.5	17.0

Table 3
Mooring line properties.

Segment	Diameter (mm)	Length (m)	Mass (kg/m)	Axial stiffness (N)
Top chain	147	50	473	9.5×10^8
Wire	124	600	63.3	1.8×10^9
Bottom chain	147	50	473	9.5×10^8

Table 4
Boundary conditions.

Boundary	Translation			Rotation		
	x	y	z	R_x	R_y	R_z
South end	Fixed	Fixed	Fixed	Fixed	Fixed	Fixed
North end	Free	Fixed	Fixed	Fixed	Fixed	Free

the mooring lines are represented by using bars submerged beneath the water surface. The pontoons are regarded as rigid bodies interacting with water. The connection between mooring lines and the pontoons in the conceptual design [23] is illustrated in Fig. 2. As it can be seen, a chain stopper is provided on the side wall of the moored pontoon. The mooring line is terminated just above the chain stopper. In the idealised floating bridge model, the fairlead points of the mooring lines are attached to the pontoon side wall at 3 m draught. Table 1 lists the sectional properties of the bridge girder and column with respect to their local axes (see Fig. 1(b)). Note that $I_{x'}$ denotes the torsional constant of the section. $I_{y'}$ and $I_{z'}$ refer to the second moments of inertia about the y' and z'-axes, respectively. $I_{x'x'}$ is the mass moment of inertia per unit length. Table 2 summarises the geometric properties of the pontoons and the radii of gyration about their local axes whose origin o' is located at the centre of gravity (see Fig. 1(b)). The mooring line properties are given in Table 3. A pretension of 1400 kN is applied to each line inside the two end clusters. For the two internal clusters, the mooring lines pretension is set to 1522 kN. These pretensions are purposely chosen such that the group stiffnesses of the four mooring clusters match those reported by Multiconsult [23]. The boundary conditions are given in Table 4. Note that the translational degree of freedom of bridge girder along the x-axis at the north end is released to allow for axial deformation due to thermal effects. Also note that all the parameters listed here are based on the independent feasibility studies of the straight floating bridge concept by Multiconsult and DNV GL [23,24].

2.2. Modelling bridge structural components

The finite element method is employed for the modelling of the structural components of the bridge, including girders, columns and mooring lines. The bridge girders and columns are discretised into three-dimensional prismatic Euler-Bernoulli beam elements. The mooring lines are modelled by using bar elements accounting for their geometric stiffness. The pontoons are modelled as rigid bodies attached to the bottom of the bridge columns. Both mooring lines and pontoons are subjected to the hydrodynamic loads defined in the next section. After transferring the beam and bar element matrices from the local axis to the global axis and assemblage, the following equations of motion of the bridge structure can be formed

$$\mathbf{M}_B\ddot{\mathbf{u}}_B + \mathbf{C}_B\dot{\mathbf{u}}_B + \mathbf{K}_B\mathbf{u}_B = \mathbf{F}_B, \tag{1}$$

herein, $\mathbf{M}_B$, $\mathbf{C}_B$, $\mathbf{K}_B$ and $\mathbf{F}_B$ are the global structural mass, damping and stiffness matrices of the floating bridge and the load vector,

respectively, $\mathbf{u}_B$ is the global displacement vector, and the superscript dots denote partial derivatives with respect to the time t.

2.3. Modelling hydrodynamic loads

Pontoons and mooring lines are the bridge components that are subjected to hydrodynamic loads. The pontoons are regarded as large volume floating bodies. The hydrodynamic coefficients may be evaluated by using the potential flow theory in the frequency domain. Due to the large spacing between adjacent pontoons, the hydrodynamic interaction is expected to be small and thus neglected. Then, the equations of motion for the floating pontoons in the time domain can be written according to Cummins theory [25] as

$$\left(\mathbf{M}_p + \mathbf{A}_p^{\infty}\right)\ddot{\mathbf{u}}_p(t) + \int_{-\infty}^{\infty} \mathbf{K}_r(t-\tau)\dot{\mathbf{u}}_p(\tau)\mathrm{d}\tau + (\mathbf{K}_b + \mathbf{K}_h)\mathbf{u}_p(t) = \mathbf{F}_{exc}(t), \tag{2}$$

where $\mathbf{M}_p$ denotes the inertia matrix of pontoon, $\mathbf{A}_p^{\infty}$ is the matrix of added mass at infinite frequency, $\mathbf{K}_r(t-\tau)$ is the retardation function representing the memory effect of the fluid, $\mathbf{K}_b$ is the stiffness matrix for the bridge structure, $\mathbf{K}_h$ is the matrix of hydrostatic restoring stiffness, $\mathbf{u}_p$ is the displacement vector of the pontoon, and $\mathbf{F}_{exc}(t)$ is the vector of wave excitation forces containing the first order and second order difference-frequency force components ($\mathbf{F}_{exc}^1$, $\mathbf{F}_{exc}^2$) that are given by

$$\mathbf{F}_{exc}^1(x,y,t) = \Re\sum_{m=1}^{N_\omega}\sum_{n=1}^{N_\theta}\left|\mathbf{H}^1(\omega_m,\theta_n)\right|\sqrt{2S_\zeta(\omega_m)D_\zeta(\theta_n)\Delta\omega\Delta\theta}\,e^{i\left(\omega_m t - k_m x\,cos(\theta_n) - k_m y\,sin(\theta_n) + \varepsilon_{mn} + \boldsymbol{\phi}_{H_{mn}^1}\right)}, \tag{3a}$$

$$\mathbf{F}_{exc}^2(x,y,t) = \Re\sum_{l=1}^{N_\omega}\sum_{m=1}^{N_\omega}\sum_{n=1}^{N_\theta}\left|\mathbf{H}^2(\omega_l,\omega_m,\theta_n)\right|\sqrt{2S_\zeta(\omega_l)D_\zeta(\theta_n)\Delta\omega\Delta\theta}\sqrt{2S_\zeta(\omega_m)D_\zeta(\theta_n)\Delta\omega\Delta\theta}\,e^{i\left((\omega_l-\omega_m)t + \varepsilon_{ln} - \varepsilon_{mn} + \boldsymbol{\phi}_{H_{lmn}^2}\right)}, \tag{3b}$$

where $\mathbf{H}^1(\omega,\theta)$ is the matrix containing the first order wave force transfer functions, $\mathbf{H}^2(\omega,\omega,\theta)$ corresponds to the second order quadratic transfer functions, $S_\zeta(\omega)$ is the unidirectional wave spectrum, $D_\zeta(\theta)$ denotes the directional distribution, k is the wave number, ε is the random phase angle of wave components, and ϕ_H is the phase angle of the wave force transfer functions, the notation $\Re$ denotes the real part of the given summation expressions. Note that in the calculation of second order difference-frequency wave forces, the effect of directional interaction between waves is not considered for the sake of simplicity.

The mooring lines are slender structures submerged in water. When they are subjected to motions, inertial and viscous forces develop on the mooring lines. The viscous forces contribute to the hydrodynamic damping of the floating bridge system. The transverse hydrodynamic load per unit length f_m exerted on these structural components may be reasonably evaluated by using the Morison equation which is expressed as

$$f_m = \rho_w V\dot{u}_w + \rho_w C_a V(\dot{u}_w - \dot{u}_m) + \frac{1}{2}\rho_w C_d D(u_w - u_m)|u_w - u_m|, \tag{4}$$

herein, ρ_w is the water density, V is the volume per unit length of the mooring line, D is the diameter of the mooring line, C_a and C_d are the added mass and quadratic drag coefficients, respectively. In this study C_a equals 1.0 and C_d is set to 2.4 for chain segments and 1.2 for wire segments [23]. u_m is the transverse velocity of the mooring line, and accordingly, u_w is the flow speed along the direction of u_m.

2.4. Modelling wave conditions

Short-term sea states are considered in this study. They may be regarded as Gaussian and stationary. The directional wave spectrum of the random wave field can be described by a product of the unidirectional wave spectrum $S_\zeta(\omega)$ and the direction distribution function $D_\zeta(\theta)$. According to the design basis for floating bridges across the Bjørnafjord [26], the JONSWAP spectrum fits the locally wind generated wave conditions and thus $S_\zeta(\omega)$ may be written as

$$S_\zeta(\omega) = \frac{5}{16}A_\gamma H_s^2\frac{\omega_p^4}{\omega^5}e^{-\frac{5}{4}\left(\frac{\omega}{\omega_p}\right)^{-4}}\gamma^{e^{-\frac{1}{2}\left(\frac{\omega-\omega_p}{\sigma\omega_p}\right)^2}}, \tag{5}$$

where $A_\gamma = 1 - 0.287\ln(\gamma)$, H_s is the significant wave height, ω_p is the peak angular frequency which equals $2\pi/T_p$, T_p is the peak period, γ is the non-dimensional peak shape parameter, and σ is the spectrum width parameter which equals 0.07 for $\omega \le \omega_p$ and 0.09 for $\omega > \omega_p$.

The directional spreading follows the cos-n distribution and thus $D_\zeta(\theta)$ is given by

$$D_\zeta(\theta) = \frac{\Gamma\left(1+\frac{n}{2}\right)}{\sqrt{\pi}\Gamma\left(\frac{1}{2}+\frac{n}{2}\right)}\cos^n(\theta-\theta_p), \tag{6}$$

where n is the spreading coefficient, and θ_p is the principal (main) wave direction. At Bjørnafjord, the wind generated waves are

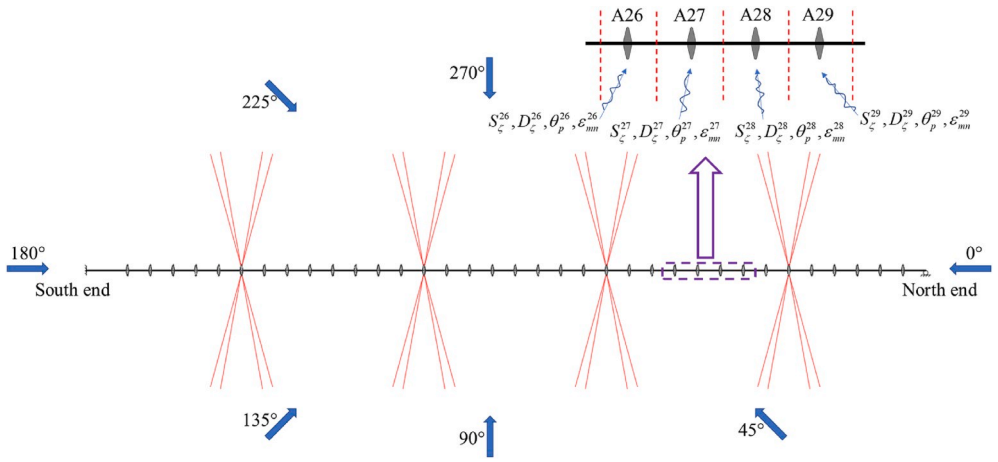

Fig. 3. Schematic plan view of floating bridge and description of wave conditions.

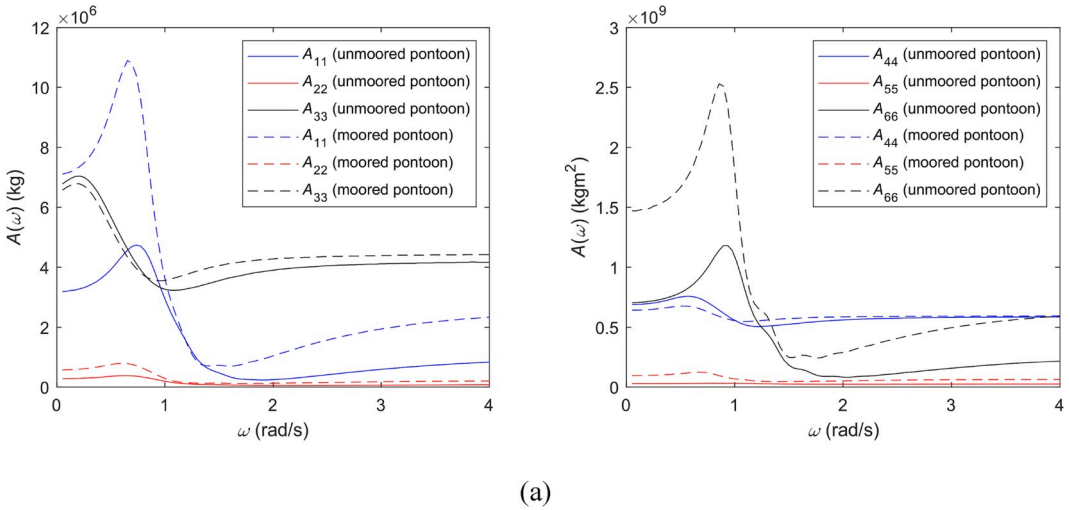

(a)

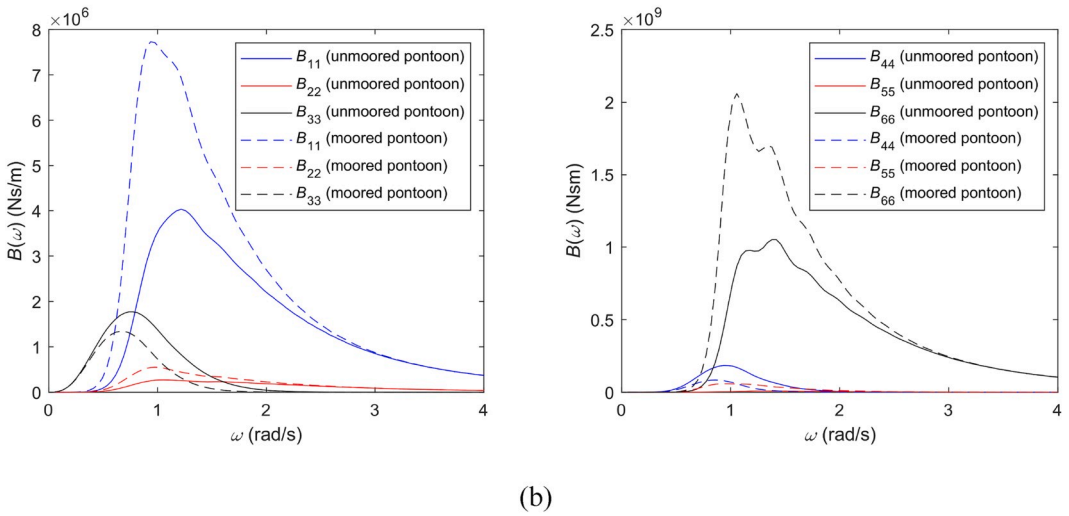

(b)

Fig. 4. Hydrodynamic coefficients of pontoons: (a) added mass and (b) potential damping.

Table 5
Design homogeneous wave conditions [26].

Return period	Wind waves			Swell		
	H_s	T_p	θ_p	H_s	T_p	θ_p
1-year	1.30 m	4.6 s	225°–315°	0.26 m	20 s	300°
100-year	2.40 m	5.9 s	225°–315°	0.40 m	20 s	300°

generally short-crested. Therefore, n may be set to 4–6 for wind seas. On the other hand, the incoming swell has low directional spreading and thus n may be chosen within the range from 10 to 20 [26]. In this study, the n value is taken as 4 and 10 for wind waves and swell, respectively.

According to Cheng et al. [13], the wave conditions at the Bjørnafjord exhibit inhomogeneity. Due to the lack of detailed description of the inhomogeneous wave conditions, one may reasonably assume that the wave conditions, i.e. $S_\zeta^i(\omega)$ and $D_\zeta^i(\theta)$, in the vicinity of an arbitrary pontoon i are homogeneous [16,27–29], as illustrated in Fig. 3. If the unidirectional wave spectrum $S_\zeta^i(\omega)$, directional distribution $D_\zeta^i(\theta)$ and random phase angle of wave components ε_{mn}^i are identical at all pontoons, the described wave conditions along the full length of the floating bridge are homogeneous. Otherwise, the wave conditions are inhomogeneous. Furthermore, if $\varepsilon_{mn}^i = \varepsilon_{mn}^j,\ \ i \neq j$ holds in an inhomogeneous wave field for arbitrary pontoon numbers i and j, the wave conditions along the entire length of the bridge are then fully coherent and correlated. On the other hand, if ε_{mn}^i is completely random at various pontoon locations, the corresponding wave conditions are incoherent as well as uncorrelated, i.e. they are independent of each other.

2.5. Numerical implementation

The boundary element method is employed for the evaluation of the hydrodynamic coefficients of pontoons in the frequency domain. The frequency dependent added mass $A(\omega)$ and potential damping $B(\omega)$ computed by using WAMIT [30] are plotted in Fig. 4. These hydrodynamic coefficients will then be used for calculation of the retardation functions for the subsequent global analysis of the floating bridge in the time domain.

The time domain finite element simulations are carried out by using the SIMA package through a coupled RIFLEX-SIMO simulation task [31,32]. In the finite element modelling of the bridge girders, each span is discretised into at least 10 elements to ensure that the modes within any span are well captured. In view of the girder element size, three elements are used to model a bridge column. Each mooring line is modelled by 45 bar elements. In addition to the hydrodynamic potential and viscous damping described in Section 2.3, the floating bridge also possesses structural damping that may be defined by using the Rayleigh damping. By assigning the mass coefficient $\mu = 0.001$ and stiffness coefficient $\lambda = 0.025$, the resulting modal damping ratio $\xi_i = 0.5(\mu/\omega_i + \lambda\omega_i)$, where ω_i is the angular frequency corresponding to the ith vibration mode, is accordingly 0.5% for the fundamental vibration modes, which complies with the design specifications in Refs. [26].

In view of the configuration of the floating bridge model, linear finite element analysis may be sufficient. Under severe environmental conditions, however, some geometric nonlinearities could still be present due to the slenderness of the bridge girder and the mooring lines. These nonlinear effects are considered by employing nonlinear analysis [31]. In the time domain analysis, the Newton-Raphson approach is adopted for the update of the geometric stiffness at each time step [31]. The Newmark constant acceleration scheme is employed for the time marching integration [33]. As a rule of thumb, the time step size Δt shall satisfy the following criterion

$$\Delta t \leq \frac{T_{\min}}{20}, \tag{7}$$

where T_{min} denotes the smallest natural period of interest. In view of the local sea state conditions [26], waves with a period below 2 s have little energy to excite dynamic bridge responses. Thus, Δt may be reasonably set to 0.1 s or below.

3. Determination of wave load cases

Field measurement of the wave conditions at the Bjørnafjord was conducted by deploying three Datawell Wave Riders (DWRs) across the fjord [13]. These three DWRs were located close to the bridge pontoons which are located at A4, A13 and A27 (which correspond to pontoon numbers 4, 13 and 17). The field measurement data show that the wave conditions at the locations of the three DWRs have different H_s and θ_p varies from 288° to 312°, indicating that inhomogeneity in the wave field exists. To examine such an effect on a straight and side-anchored floating bridge, a proper description of the inhomogeneous wave conditions is critical as an input for the bridge response analysis. Additionally, it is important to set up appropriate homogeneous wave load cases for the basis of comparison. Table 5 lists the design wave load cases specified in the design basis [26] with a principal wave direction in the sector of 225°–315°. Note that a common practice in an engineering design is to apply the worst wave condition to the entire bridge structure. In view of this, inhomogeneous wave load cases may be reasonably established by scaling up the significant wave heights H_s and peak periods T_p measured at the three DWRs such that the highest inhomogeneous H_s and T_p equal the homogeneous wave characteristics listed in Table 5. Due to the lack of further information, the wave inhomogeneity between the DWRs is assumed to be linearly varied

Table 6
Inhomogeneous wave conditions.

Location	Condition 1 (1-year)			Condition 2 (100-year)			Condition 3 (100-year)					
	Wind waves			Wind waves			Wind waves			Swell		
	H_s (m)	T_p (s)	θ_p (°)	H_s (m)	T_p (s)	θ_p (°)	H_s (m)	T_p (s)	θ_p (°)	H_s (m)	T_p (s)	θ_p (°)
A1	1.17	4.6	314.3	2.15	5.9	314.3	1.71	3.9	288	0.09	20	300
A2	1.17	4.6	313.6	2.16	5.9	313.6	1.71	3.9	288	0.09	20	300
A3	1.17	4.6	312.8	2.16	5.9	312.8	1.71	3.9	288	0.09	20	300
A4	1.17	4.6	312.0	2.16	5.9	312.0	1.71	3.9	288	0.09	20	300
A5	1.17	4.6	311.2	2.17	5.9	311.2	1.71	3.9	288	0.09	20	300
A6	1.18	4.6	310.4	2.17	5.9	310.4	1.71	3.9	288	0.09	20	300
A7	1.18	4.6	309.7	2.18	5.9	309.7	1.71	3.9	288	0.09	20	300
A8	1.18	4.6	308.9	2.18	5.9	308.9	1.71	3.9	288	0.09	20	300
A9	1.18	4.6	308.1	2.19	5.9	308.1	1.63	3.9	288	0.15	20	300
A10	1.19	4.6	307.3	2.19	5.9	307.3	1.63	3.9	288	0.15	20	300
A11	1.19	4.6	306.6	2.20	5.9	306.6	1.63	3.9	288	0.15	20	300
A12	1.19	4.6	305.8	2.20	5.9	305.8	1.63	3.9	288	0.15	20	300
A13	1.19	4.6	305.0	2.20	5.9	305.0	1.63	3.9	288	0.15	20	300
A14	1.20	4.6	303.8	2.22	5.9	303.8	1.63	3.9	288	0.15	20	300
A15	1.21	4.6	302.6	2.23	5.9	302.6	1.63	3.9	288	0.15	20	300
A16	1.22	4.6	301.4	2.25	5.9	301.4	1.63	3.9	288	0.15	20	300
A17	1.22	4.6	300.1	2.26	5.9	300.1	1.63	3.9	288	0.15	20	300
A18	1.23	4.6	298.9	2.27	5.9	298.9	2.06	5.2	288	0.31	20	300
A19	1.24	4.6	297.7	2.29	5.9	297.7	2.06	5.2	288	0.31	20	300
A20	1.25	4.6	296.5	2.30	5.9	296.5	2.06	5.2	288	0.31	20	300
A21	1.25	4.6	295.3	2.32	5.9	295.3	2.06	5.2	288	0.31	20	300
A22	1.26	4.6	294.1	2.33	5.9	294.1	2.06	5.2	288	0.31	20	300
A23	1.27	4.6	292.9	2.34	5.9	292.9	2.06	5.2	288	0.31	20	300
A24	1.28	4.6	291.6	2.36	5.9	291.6	2.06	5.2	288	0.31	20	300
A25	1.29	4.6	290.4	2.37	5.9	290.4	2.06	5.2	288	0.31	20	300
A26	1.29	4.6	289.2	2.39	5.9	289.2	2.06	5.2	288	0.31	20	300
A27	1.30	4.6	288.0	2.40	5.9	288.0	2.40	5.9	288	0.40	20	300
A28	1.29	4.6	285.8	2.39	5.9	285.8	2.40	5.9	288	0.40	20	300
A29	1.29	4.6	283.5	2.37	5.9	283.5	2.40	5.9	288	0.40	20	300
A30	1.28	4.6	281.3	2.36	5.9	281.3	2.40	5.9	288	0.40	20	300
A31	1.27	4.6	279.0	2.34	5.9	279.0	2.40	5.9	288	0.40	20	300
A32	1.26	4.6	276.8	2.33	5.9	276.8	2.40	5.9	288	0.40	20	300
A33	1.25	4.6	274.5	2.32	5.9	274.5	2.40	5.9	288	0.40	20	300
A34	1.25	4.6	272.3	2.30	5.9	272.3	2.40	5.9	288	0.40	20	300
A35	1.24	4.6	270.0	2.29	5.9	270.0	2.40	5.9	288	0.40	20	300

Table 7
Load cases and descriptions.

Number	Description			
	Return period	Wind sea condition	Swell condition	Wave correlation
LC1.1a	1-year	$\boldsymbol{H_s = 1.3}$ **m,** $\boldsymbol{T_p = 4.6}$ **s,** $\boldsymbol{\theta_p = 288}$°	–	**Fully correlated**
LC1.1b	1-year	$\boldsymbol{H_s = 1.23}$ **m,** $\boldsymbol{T_p = 4.6}$ **s,** $\boldsymbol{\theta_p = 288}$°	–	**Fully correlated**
LC1.2	1-year	$H_s = 1.3$ m, $T_p = 4.6$ s, $\theta_p = 288$°	–	Uncorrelated
LC1.3	1-year	Condition 1	–	Fully correlated
LC1.4	1-year	Condition 1	–	Uncorrelated
LC2.1a	100-year	$\boldsymbol{H_s = 2.4}$ **m,** $\boldsymbol{T_p = 5.9}$ **s,** $\boldsymbol{\theta_p = 288}$°	–	**Fully correlated**
LC2.1b	100-year	$\boldsymbol{H_s = 2.27}$ **m,** $\boldsymbol{T_p = 5.9}$ **s,** $\boldsymbol{\theta_p = 288}$°	–	**Fully correlated**
LC2.2	100-year	$H_s = 2.4$ m, $T_p = 5.9$ s, $\theta_p = 288$°	–	Uncorrelated
LC2.3	100-year	Condition 2	–	Fully correlated
LC2.4	100-year	Condition 2	–	Uncorrelated
LC3.1a	100-year	$\boldsymbol{H_s = 2.4}$ **m,** $\boldsymbol{T_p = 5.9}$ **s,** $\boldsymbol{\theta_p = 288}$°	$H_s = 0.4$ m, $T_p = 20$ s, $\theta_p = 300$°	**Fully correlated**
LC3.1b	100-year	$\boldsymbol{H_s = 2.27}$ **m,** $\boldsymbol{T_p = 5.9}$ **s,** $\boldsymbol{\theta_p = 288}$°	$H_s = 0.24$ m, $T_p = 20$ s, $\theta_p = 300$°	**Fully correlated**
LC3.2	100-year	$H_s = 2.4$ m, $T_p = 5.9$ s, $\theta_p = 288$°	$H_s = 0.4$ m, $T_p = 20$ s, $\theta_p = 300$°	Uncorrelated
LC3.3	100-year	Condition 3	Condition 3	Fully correlated
LC3.4	100-year	Condition 3	Condition 3	Uncorrelated

*Load cases highlighted by using bold fonts correspond to homogeneous wave conditions.

[16].

Table 6 shows three inhomogeneous wave conditions to be considered in this study. The first two are the 1-year and 100-year inhomogeneous wave conditions established based on the field measurement data collected at the Bjørnafjord [13]. Due to availability of data, only wind waves are accounted for. As it can be seen, the waves described in these two conditions exhibit a relatively

Table 8
Fundamental natural periods of floating bridge.

Mode number	Dominating axis	Natural period	Natural period [23]
Mode 1	*y*-axis (transverse displacement)	34.1 s	34.4 s
Mode 2	*y*-axis	31.2 s	30.9 s
Mode 3	*y*-axis	30.3 s	29.0 s
Mode 4	*y*-axis	20.1 s	21.2 s
Mode 5	*y*-axis	15.5 s	15.1 s
Mode 7	*x*-axis (axial displacement)	11.6 s	Not reported
Mode 9	*x*-axis	11.6 s	Not reported
Mode 11	*x*-axis	11.6 s	Not reported
Mode 13	*x*-axis	11.6 s	Not reported
Mode 15	*x*-axis	11.5 s	Not reported
Mode 41	*z*-axis (vertical displacement)	7.2 s	7.4 s
Mode 44	*z*-axis	7.0 s	7.0 s
Mode 46	*z*-axis	6.7 s	6.8 s
Mode 47	*z*-axis	6.6 s	6.4 s
Mode 48	*z*-axis	6.6 s	6.3 s

large spatial variation in θ_p with a minor inhomogeneity in H_s and a constant T_p. Thus, examining these two wave conditions is expected to reveal the effect of inhomogeneity in the wave direction on the bridge responses under both operational and ultimate wave conditions. The third condition describes a different pattern of 100-year inhomogeneous waves established based on the wave conditions at the Sulafjord [34]. When compared with the first two conditions, θ_p remains unchanged in condition 3. But a much larger inhomogeneity in H_s and T_p is present and its effect may be revealed by comparing with the corresponding homogeneous wave conditions. Furthermore, inhomogeneous swell with a longer T_p that may give excitation to the lower order vibration modes of the floating bridge is also accounted for in condition 3.

Table 7 summarises the wave load cases to be examined in this study. There are three main load cases (LCs), namely LC1, LC2 and LC3 that correspond to the wave conditions listed in Table 6. Each LC is comprised of three inhomogeneous wave load cases and one homogeneous wave load case that serves as a basis for comparison with the inhomogeneous wave load cases. The homogeneous wave load cases (LC1.1, LC2.1 and LC3.1) are further categorised into sub-cases a and b. Case a is defined by using the parameters listed in the design bases [26] and Table 5, whereas the H_s in case b is scaled down to match the average H_s in an inhomogeneous wave condition. The latter describes a sea state with the same wave energy as in the inhomogeneous wave load case provided that T_p remains unchanged. In all case studies, five independent wave realisations of each load case are used to reduce the variations in the stochastic results. In addition to the wave inhomogeneities described in Table 7, this study also investigates various wave effects, including short-crestedness of wind waves and the first and second order wave load effects. Note that, unless otherwise stated, the wind waves are short-crested, and the *n*-value stated in Section 2.4 is employed throughout this study.

4. Numerical analysis

4.1. Identification of modal properties

The floating bridge is a complex structural system with many vibration modes that may be excited by the wave loads. Therefore, it is important to identify the natural periods and mode shapes before performing stochastic dynamic simulations. Table 8 shows the natural periods of the first five modes along the global *x*, *y* and *z* axes computed by using the proposed idealised and generic bridge model. For the purpose of comparison, Table 8 also lists the natural periods reported by Multiconsult [23] in their independent study on the design concept that comprises the cable-stayed bridge section and the high part of the floating bridge section (see Fig. 1(a)). As it can be seen, a very good agreement is found between the natural periods evaluated by using the two models. This suggests that the proposed idealised bridge model shown in Fig. 1(b) can well capture the essential dynamic characteristics of the design concept. Note that the identified longest natural period is 34.1 s. As a reference, the alternative curved floating bridge design concept possesses a much longer fundamental period of 56 s [15]. Clearly, the presence of the mooring lines effectively increases the transverse stiffness of the straight bridge.

Fig. 5 shows the lowest transverse, axial and vertical vibration mode shapes of the bridge girder. As it can be seen, the lowest transverse vibration modes of the bridge girder have long natural periods ranging from 11.5 s to 34.1 s. As a result, these modes may be excited by the second order wave drift forces and swell loads. Thus, the transverse displacement of the bridge is expected to be significantly affected by these slowly varying wave loads. Note that these transverse vibration modes are also found to be coupled with the torsional modes due to the effect of the mooring clusters. The natural periods of the lowest axial modes are clustered around 11 s. Essentially, all these mode shapes correspond to the first order axial mode, similar to that of a cantilever beam, but coupled with different vertical vibrations of the bridge girder near the clusters of mooring lines. This is because the mooring lines also restrain the axial deformation of the bridge girders. However, as they are away from the wave periods, the level of excitation is expected to be low. The lowest vertical vibration modes of the bridge girder are found to be densely distributed between 6.2 s and 7.2 s. These modes are very close to the peak periods of the design wind waves. Consequently, the vertical responses of the bridge girder are expected to be governed by the first order wave loads in a wind sea.

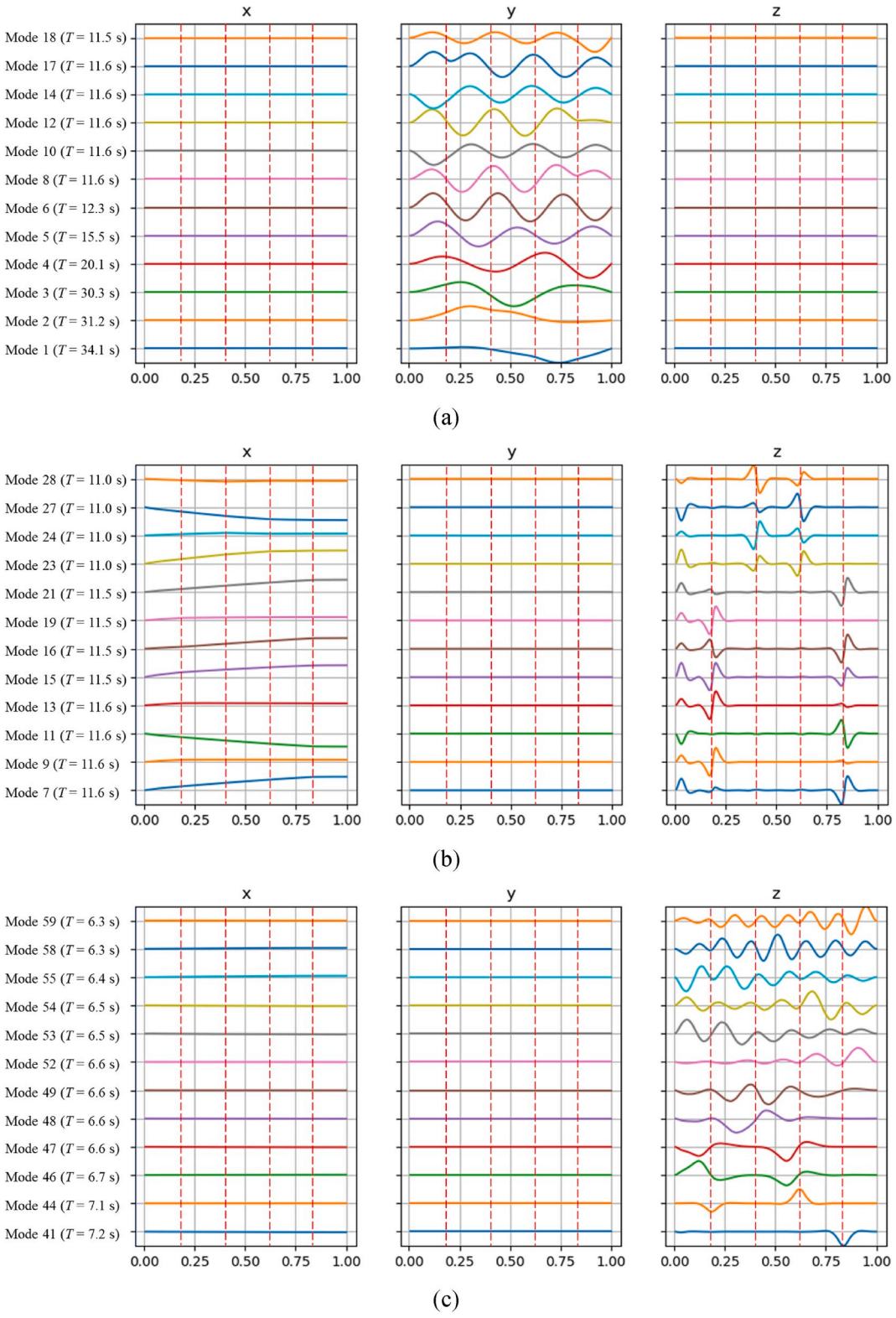

Fig. 5. Mode shapes of bridge girder with dominating displacement along (a) y-axis, (b) x-axis and (c) z-axis (See coordinate system in Fig. 1). Dashed red lines denote the location of mooring clusters. (For interpretation of the references to colour in this figure legend, the reader is referred to the Web version of this article.)

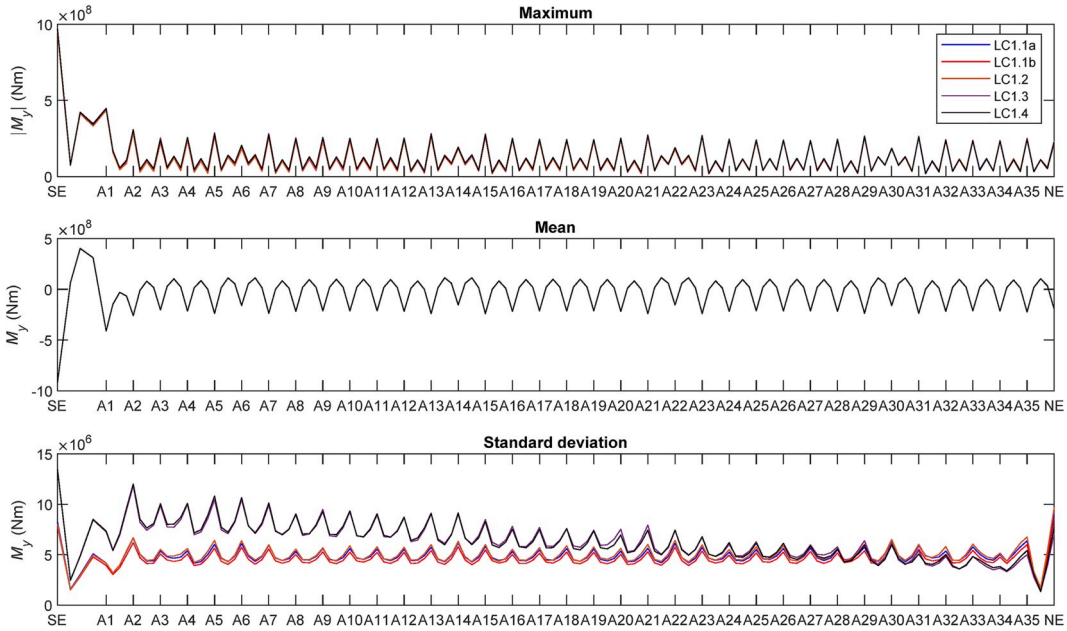

Fig. 6. Statistical values of weak axis bending moment under 1-year wave load cases (LC1).

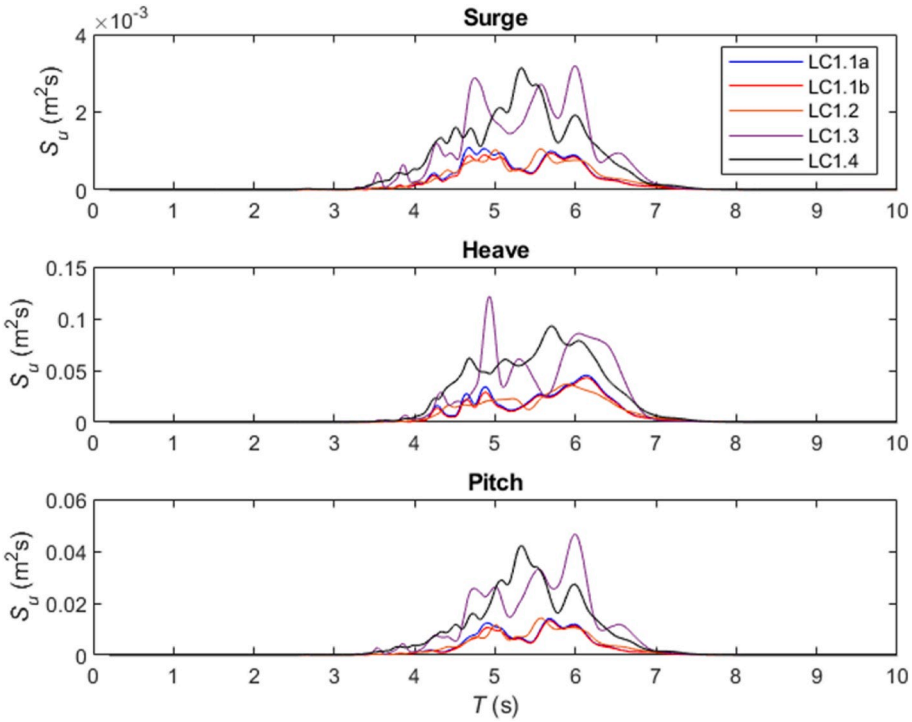

Fig. 7. Motion response spectra of pontoon at A2 under 1-year wave load cases (LC1).

4.2. 1-year wave load effects (LC1)

This section presents the results of the dynamic responses of the floating bridge under 1-year wave load cases. As the girder is the key structural component of the floating bridge, its responses in terms of forces and motions which develop under wave actions are the focus of the study. As the boundary conditions allow for axial deformation of the bridge girder and the axial modes are sufficiently away from the wave periods, the axial responses of the bridge are found to be much smaller than that of a curved bridge [15,16]. In

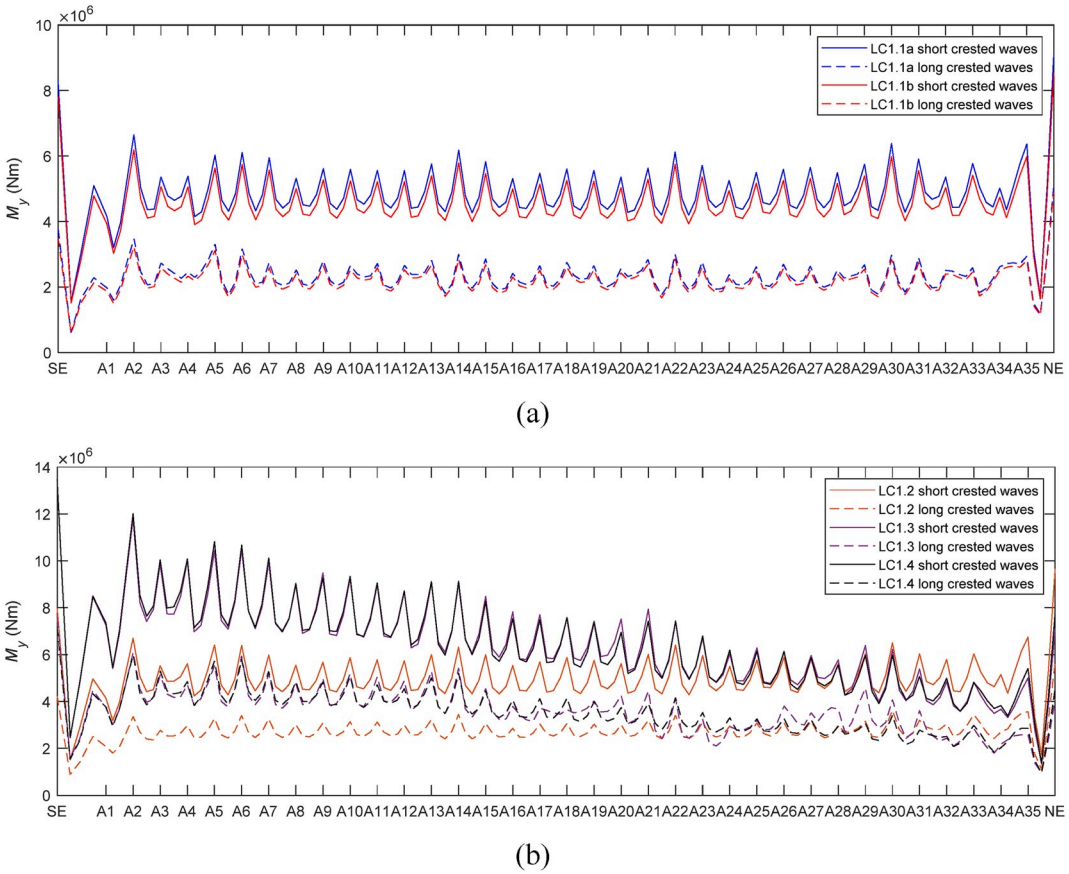

Fig. 8. Effect of wave short-crestedness on standard deviation of weak axis bending moment under 1-year wave load cases (LC1): (a) homogeneous waves and (b) inhomogeneous waves.

addition, the torsional moments are also found to be much lower when compared with a curved bridge [15,16] due to the restraint of mooring lines and the lack of coupling between torsional and vertical responses in a straight bridge. For these reasons, the focus is placed on the bending moments and transverse motions of the bridge girder.

Fig. 6 shows the statistical results regarding the weak axis bending moment M_y along the entire length of the bridge girder under 1-year wave loads. In general, the maximum and mean values of M_y are dominated by the self-weight of the bridge. The standard deviations in M_y, caused by the dynamic wave effects, are rather similar for LC1.1a and LC1.1b. This is due to the fact that the difference in H_s between the two homogeneous wave load cases is pretty small. When compared with LC1.2, the difference in the standard deviation is also small. Similarly, the results for LC1.3 and LC1.4 are very close to each other. This suggests that the coherence between waves at different pontoon locations has a negligible effect on M_y. However, the dynamic weak axis bending moments caused by the inhomogeneous wave load cases LC1.3 and LC1.4 are found to be significantly higher than the homogeneous wave load cases (LC1.1a and LC1.1b), especially for the segment between the south end and A27. This implies that the spatial variation of wave direction has a strong effect on M_y.

To reveal the reason for such a discrepancy, motion response spectra for the pontoon at location A2 are plotted in Fig. 7. Note that the power spectral density is plotted with respect to the wave period for the purpose of easy reference to the natural periods of the floating bridge. Also note that this way of presentation is used throughout the paper. Unlike $\theta_p = 288^\circ$ for homogeneous wave load cases, which is close to a beam sea condition, the inhomogeneous waves in LC1.3 and LC1.4 near the south end of the bridge are more oblique with $\theta_p > 300^\circ$. Under such circumstances, they are found to induce larger surge (translation along x-axis), heave (translation along z-axis) and pitch (rotation about (y-axis) motions of the pontoon than homogeneous waves, which amplifies the weak axis bending of the bridge girder. After A27, the principal wave directions in LC1.3 and LC1.4 are almost perpendicular to the longitudinal axis of the bridge girder. Consequently, the inhomogeneous waves would induce smaller motions of the pontoons and thus imply lower dynamic variations in M_y as compared to the homogeneous wave load cases.

Note that in Fig. 6, the wind waves are modelled as short-crested waves with a small directional distribution exponent $n = 4$ [26]. To reveal the effect of wave short-crestedness on the bridge responses, Fig. 8 plots the standard deviation of M_y due to unidirectional long-crested waves for comparison with short-crested waves. As it can be seen, short-crested waves result in a much larger M_y along the full length of the bridge for both homogeneous and inhomogeneous wave load cases. The differences are up to 176% for homogeneous

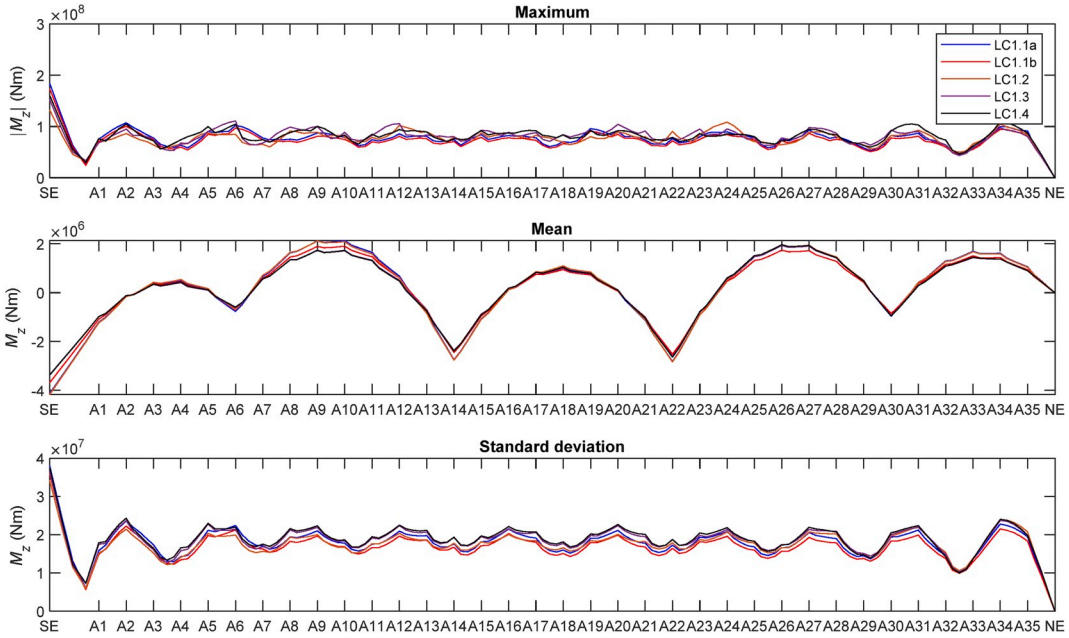

Fig. 9. Statistical values of strong axis bending moment under 1-year wave load cases (LC1).

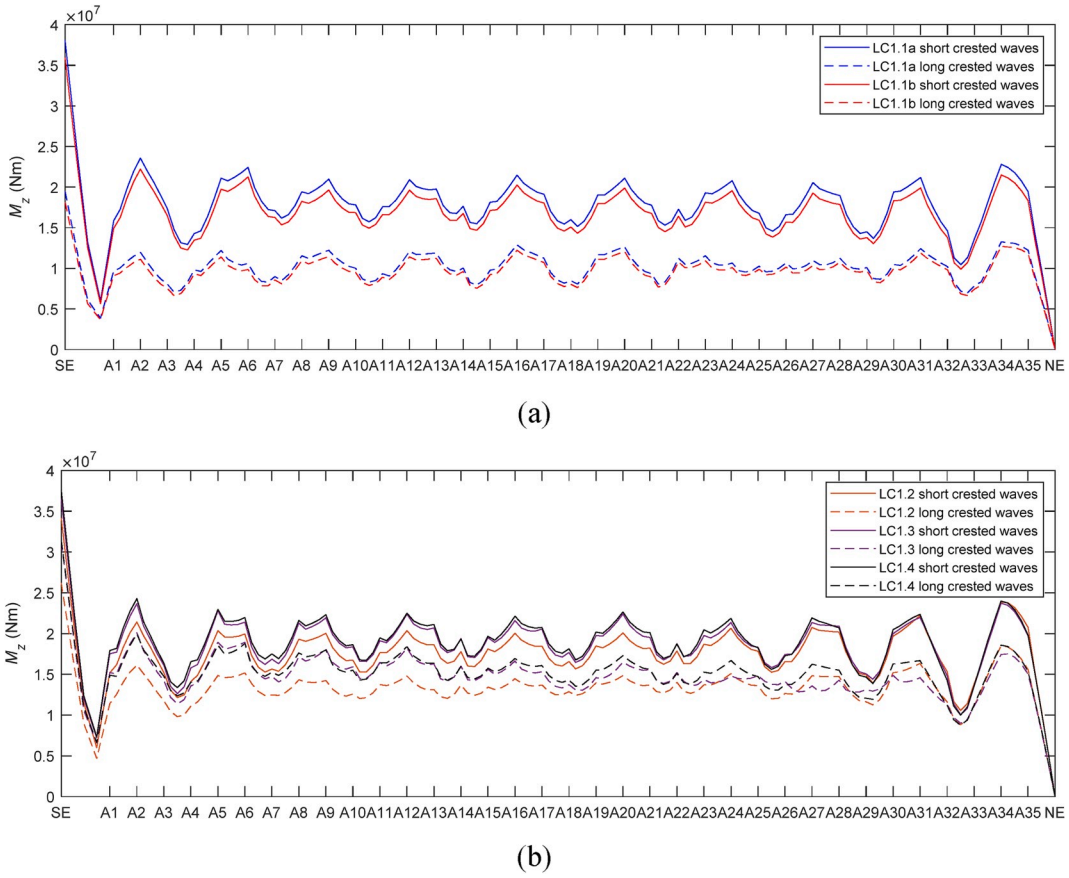

Fig. 10. Effect of wave short-crestedness on standard deviation of strong axis bending moment under 1-year wave load cases (LC1): (a) homogeneous waves and (b) inhomogeneous waves.

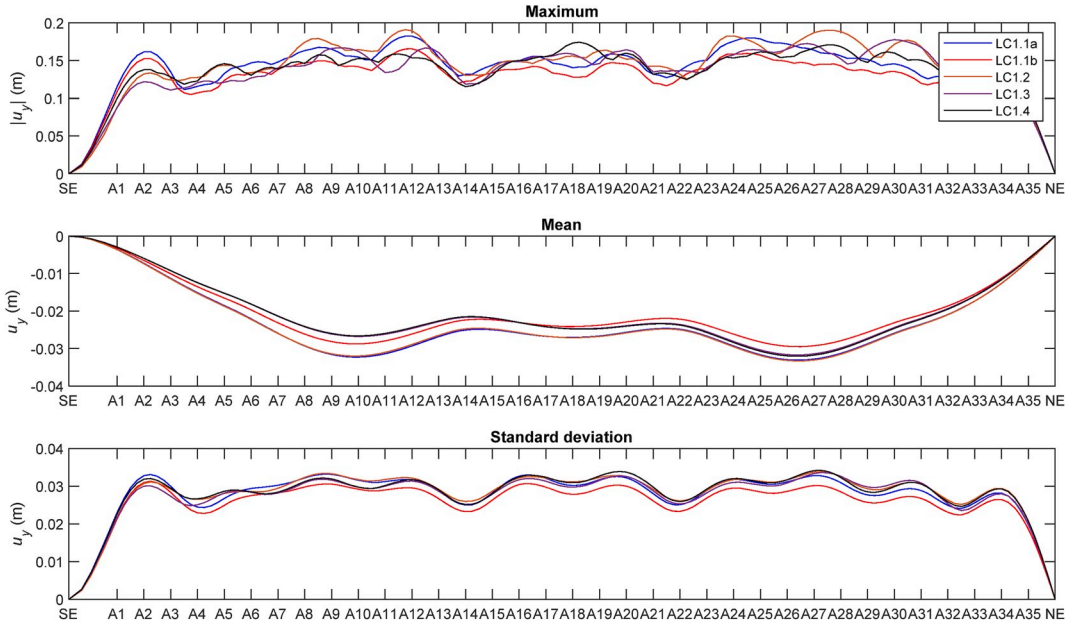

Fig. 11. Statistical values of transverse displacement under 1-year wave load cases (LC1).

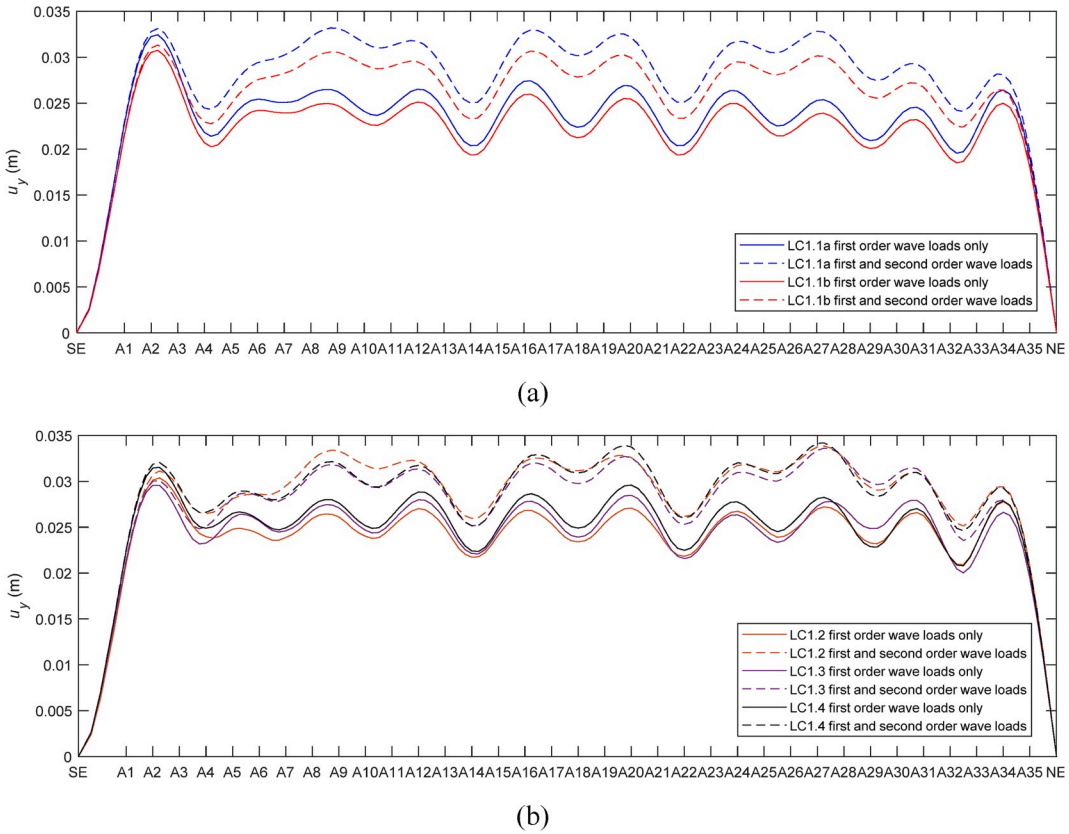

Fig. 12. Effect of wave load components on standard deviation of transverse displacement under 1-year wave load cases (LC1): (a) homogeneous waves and (b) inhomogeneous waves.

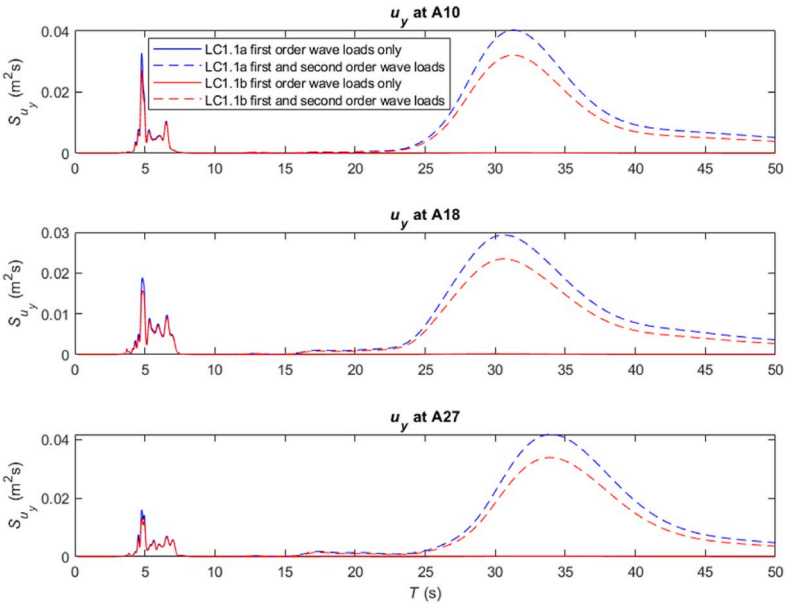

(a)

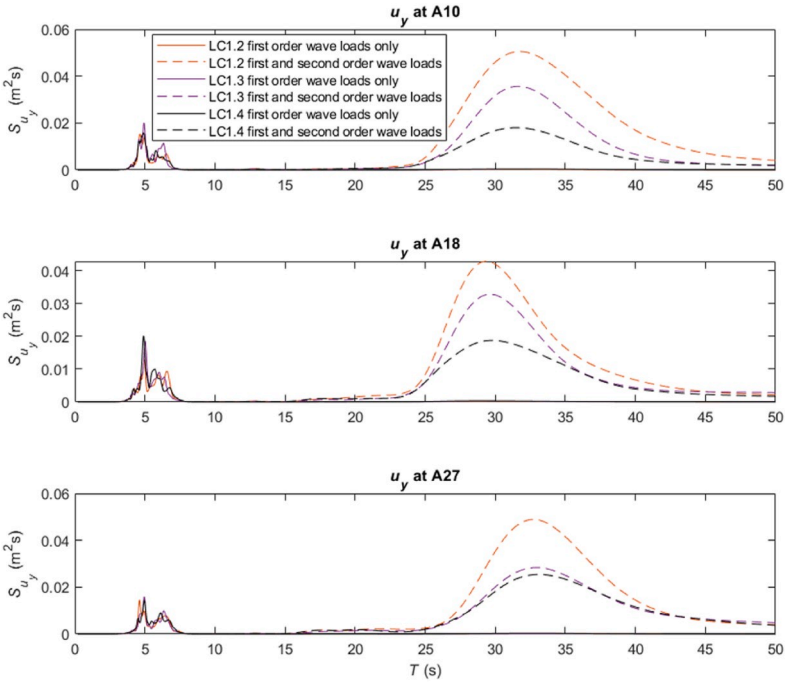

(b)

Fig. 13. Response spectra of transverse displacement under 1-year wave load cases (LC1): (a) homogeneous waves and (b) inhomogeneous waves.

waves and 129% for inhomogeneous waves. This implies that oblique wave components in short-crested waves significantly augment the weak axis bending moment of the girder when compared with long-crested waves in a near beam sea condition.

The statistical results of the strong axis bending moment M_z presented in Fig. 9 show that the wave inhomogeneity has a small

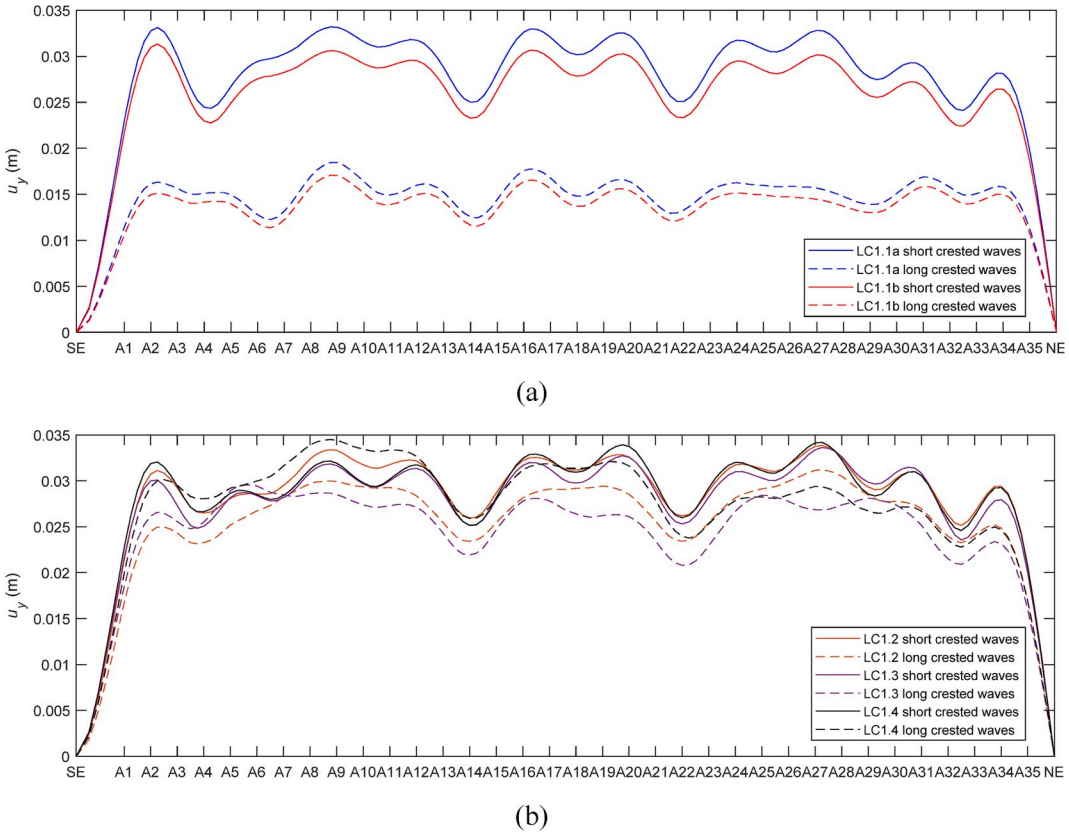

Fig. 14. Effect of wave short-crestedness on standard deviation of transverse displacement under 1-year wave load cases (LC1): (a) homogeneous waves and (b) inhomogeneous waves.

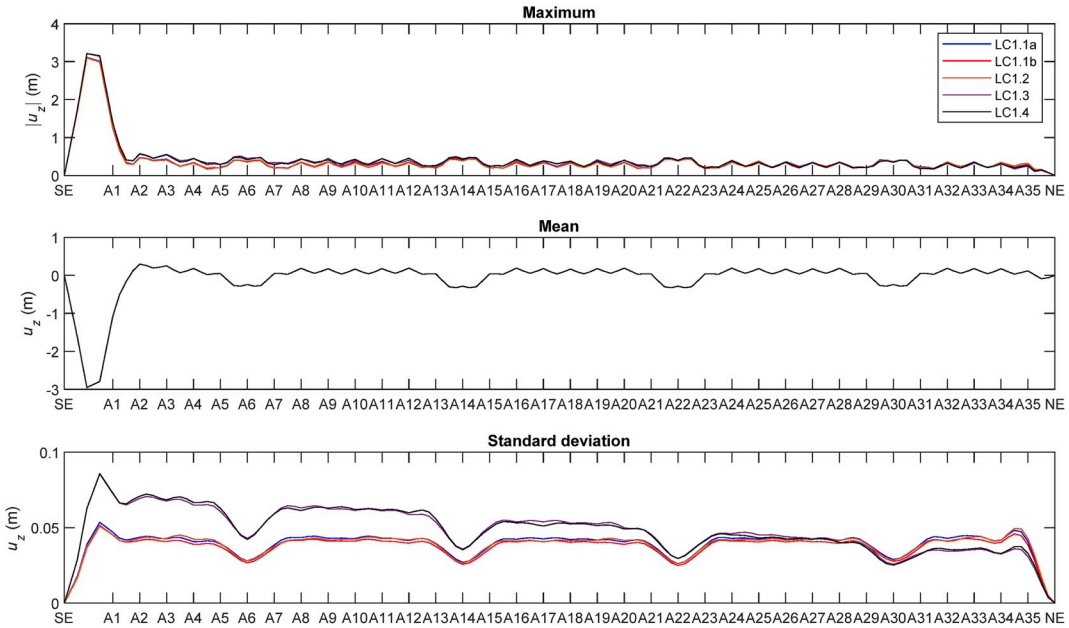

Fig. 15. Statistical values of vertical displacement under 1-year wave loads (LC1).

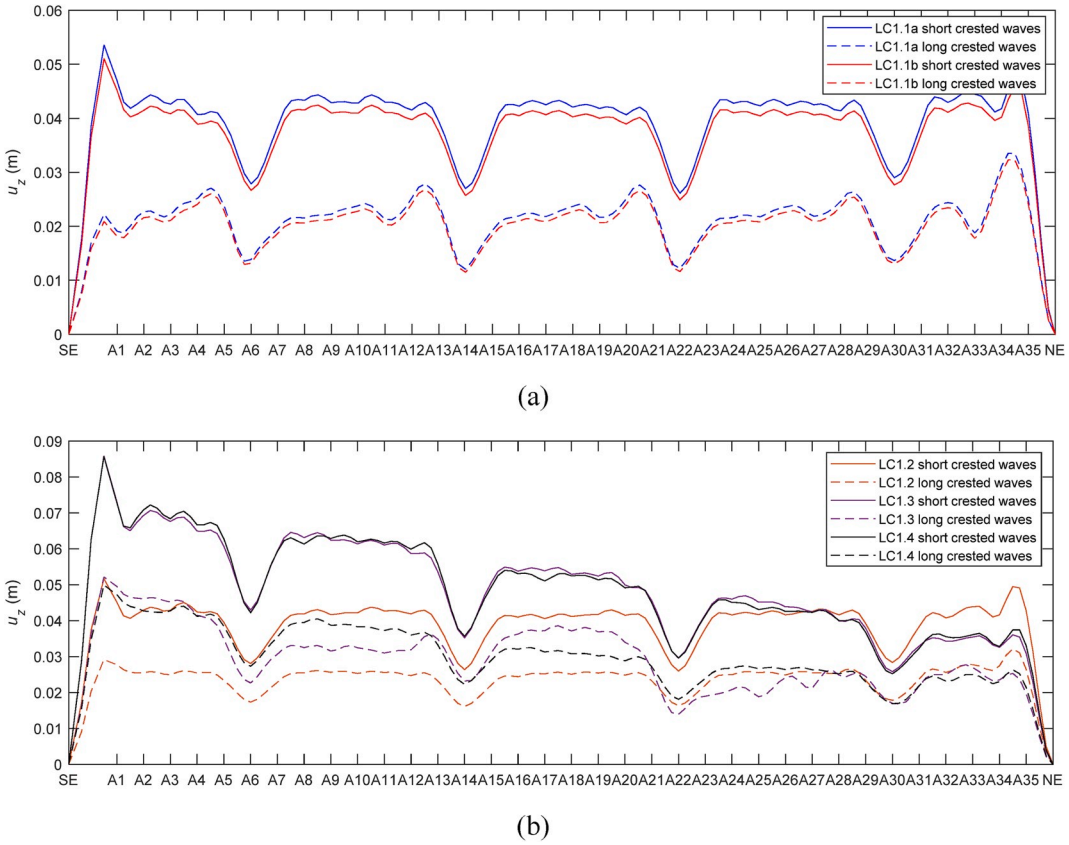

Fig. 16. Effect of wave short-crestedness on standard deviation of vertical displacement under 1-year wave load cases (LC1): (a) homogeneous waves and (b) inhomogeneous waves.

effect, although inhomogeneous wave loads tend to result in a slightly larger M_z. The effect of wave short-crestedness on M_z is also examined and shown in Fig. 10. As observed, M_z is much larger when waves are short-crested for the homogeneous wave load cases. The difference is up to 123%. This is found to substantially reduce to a maximum increase of 63% for inhomogeneous wave load cases where a spatial variation of θ_p has already be accounted for. In addition, the effect of coherence and correlation between waves at different pontoon locations on the bridge's strong axis bending moment is found to be rather small.

1-year design wave conditions are usually employed to examine the operational performance of the bridge structure under a serviceability limit state. The motions are important criteria in determining the comfort level of vehicles driving on the floating bridge. Thus, it is important to compare the girder motions under homogeneous and inhomogeneous wave loads. Fig. 11 shows the statistical results of the transverse displacement u_y of the bridge girder. The mean values are expected to be governed by the slow varying second order wave loads. In all cases, the effect of wave inhomogeneity on the transverse displacement is found to be small. Fig. 12 shows the effect of wave load components (i.e. first order wave-frequency versus second order difference-frequency load components) on the girder's dynamic transverse displacement. As it can be seen, the second order wave loads augment the standard deviation of transverse displacement considerably. To further reveal the effect of the second order wave load components, motion response spectra of the girder at A10, A18 and A27 are plotted in Fig. 13. Clearly, the second order difference-frequency wave loads excite the fundamental bridge vibration modes. The modes excited are the second, third and first transverse vibration modes, respectively, at the three girder locations. The effect of wave short-crestedness is also examined and is presented in Fig. 14. The results show that short-crested waves lead to a much larger transverse displacement of the bridge girder than long-crested waves for homogeneous wave load cases. When it comes to inhomogeneous wave load cases, however, the effect of wave short-crestedness is much smaller as a spatial variation of θ_p has already been accounted for.

Fig. 15 shows the vertical motion statistics of the bridge girder under 1-year wave loads. As it can be seen, the maximum and mean values of the vertical displacement are very similar for all load cases; they are dominated by the self-weight of the bridge. It should be mentioned that the segment between the south end and A1, which corresponds to the cable-stayed bridge in the design concept, experiences much larger vertical displacement than the other parts of the bridge. This is due to the neglection of stay cables for the sake of simplification in the idealised bridge model. However, the length of this segment has been carefully adjusted to ensure that the modal properties of the idealised bridge model match well with those of the design concept. The standard deviation of the results shows that the vertical displacement near the south end is much larger for inhomogeneous wave load cases LC1.3 and LC1.4. This is expected in view of the fact that oblique waves for inhomogeneous wave load cases (LC1.3 and LC1.4) have resulted in larger heave motions of

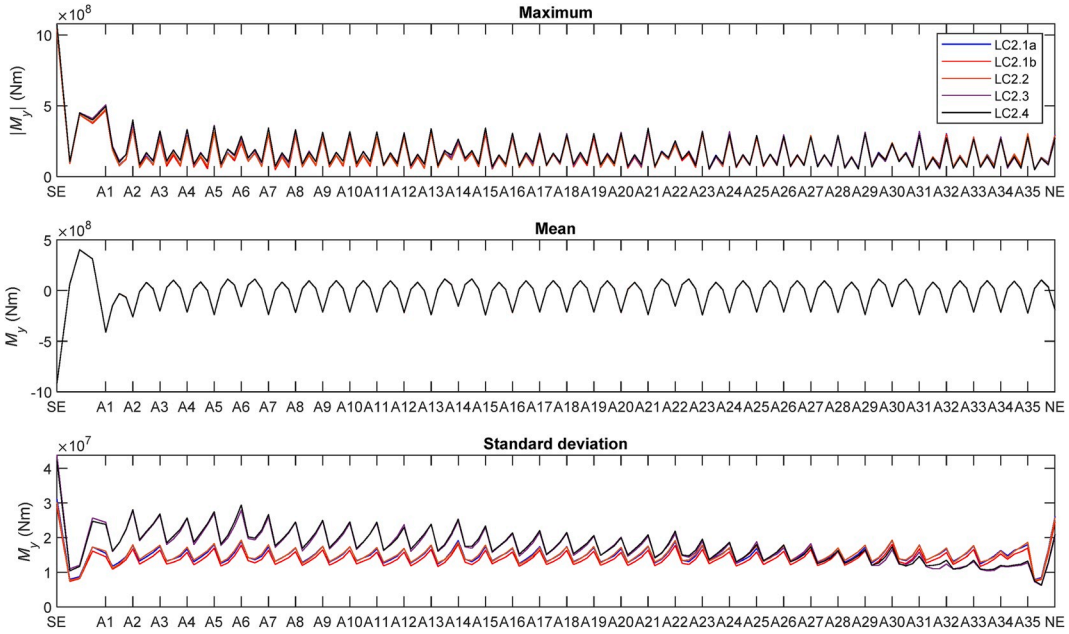

Fig. 17. Statistical values of weak axis bending moment under 100-year wave loads (LC2).

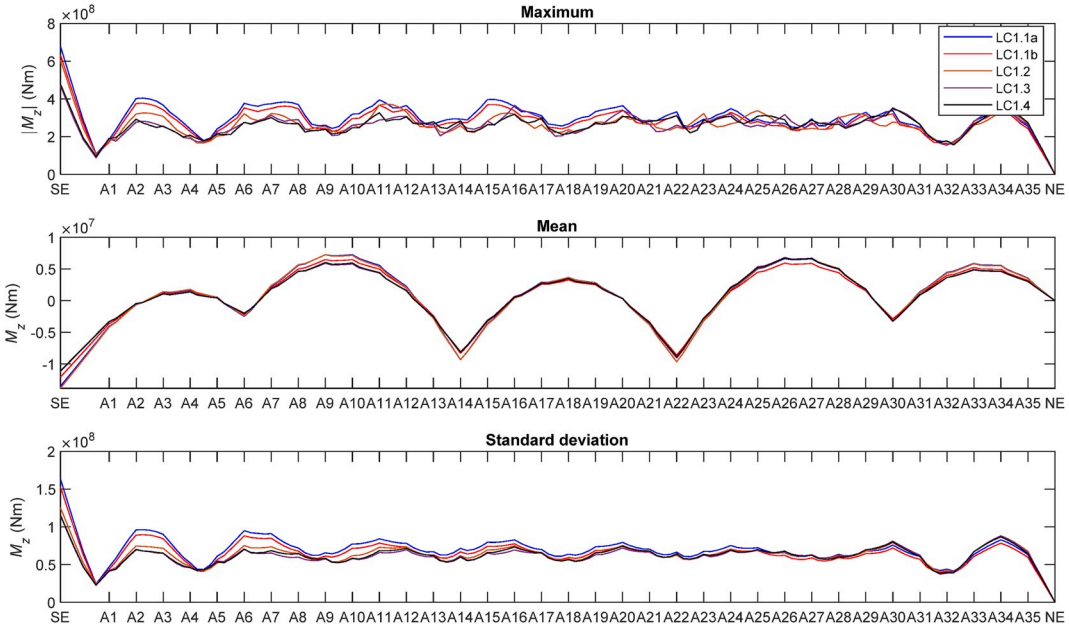

Fig. 18. Statistical values of strong axis bending moment under 100-year wave loads (LC2).

the pontoon near the south end (see Fig. 7). The difference between homogeneous and inhomogeneous load cases reduces due to the decreasing obliquity of inhomogeneous waves as the location moves toward A27. After this location, homogeneous wave load cases are found to result in larger standard deviations of the vertical displacement. Fig. 16 highlights the effect of wave short-crestedness on the standard deviation of vertical girder displacement. The results show that this standard deviation is significantly affected by the wave short-crestedness. In addition, the effect of coherence and correlation of waves at different pontoon locations is found to affect the dynamic vertical displacement, particularly for homogeneous long-crested wave load cases. For short-crested waves, however, this effect is found to be small regardless of the inhomogeneity in the wave conditions.

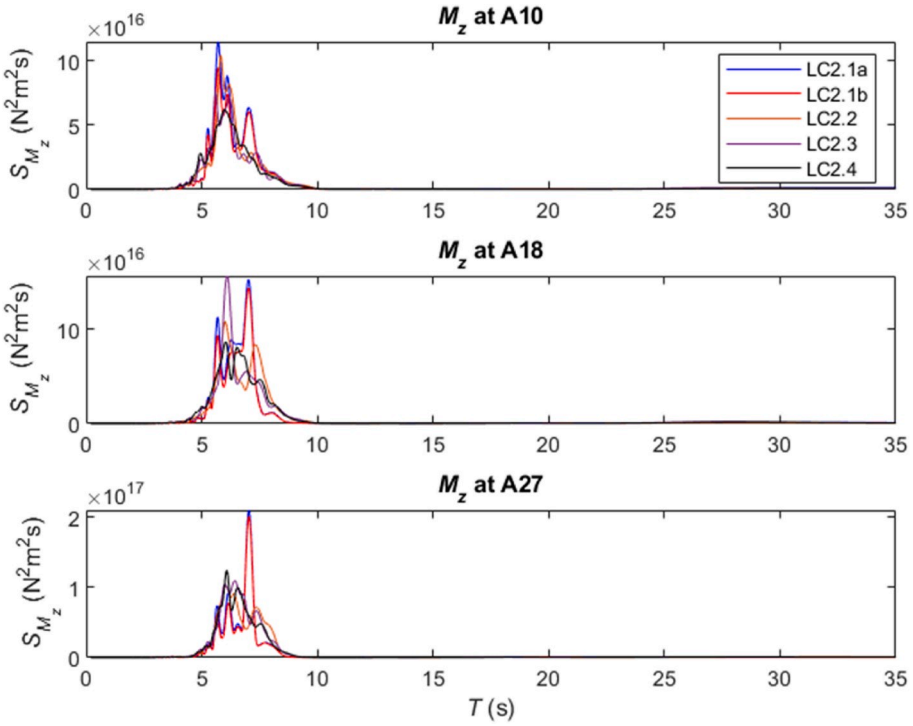

Fig. 19. Response spectra of strong axis bending moment under 10-year wave load cases (LC2).

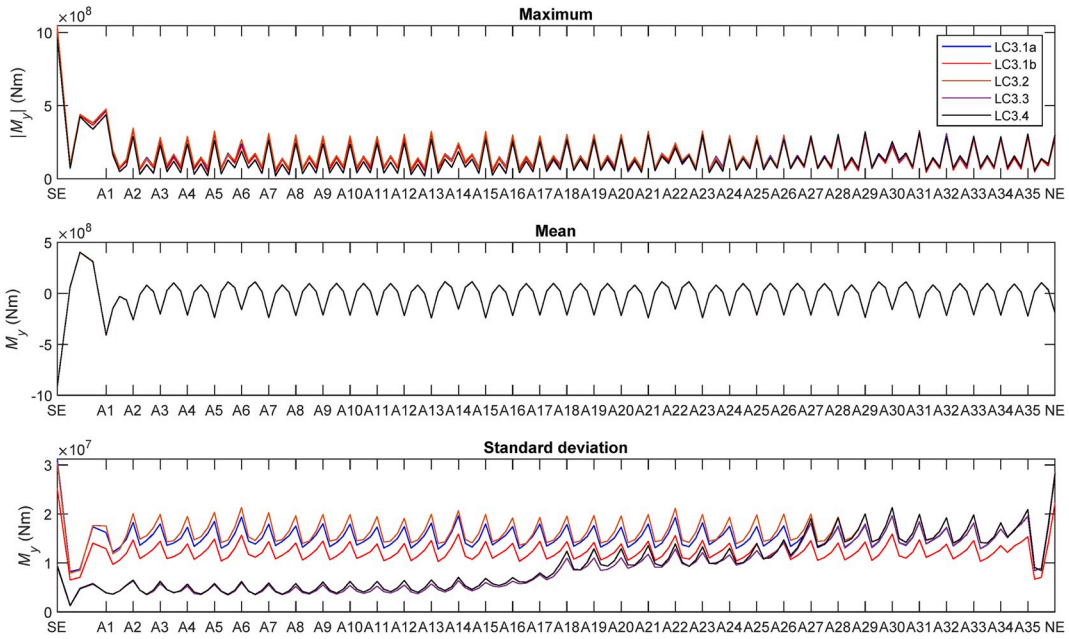

Fig. 20. Statistical values of weak axis bending moment under 100-year wave loads (LC3).

4.3. 100-year wave load effects (LC2)

The bridge responses under 100-year wave loads (LC2) are next investigated. For the sake of conciseness, the following study focuses on the effect of wave inhomogeneity in 100-year waves on the bridge responses. The effects of wave short-crestedness and the first and second order wave loads have been discussed in the previous section and are thus omitted here. Note that from this and section

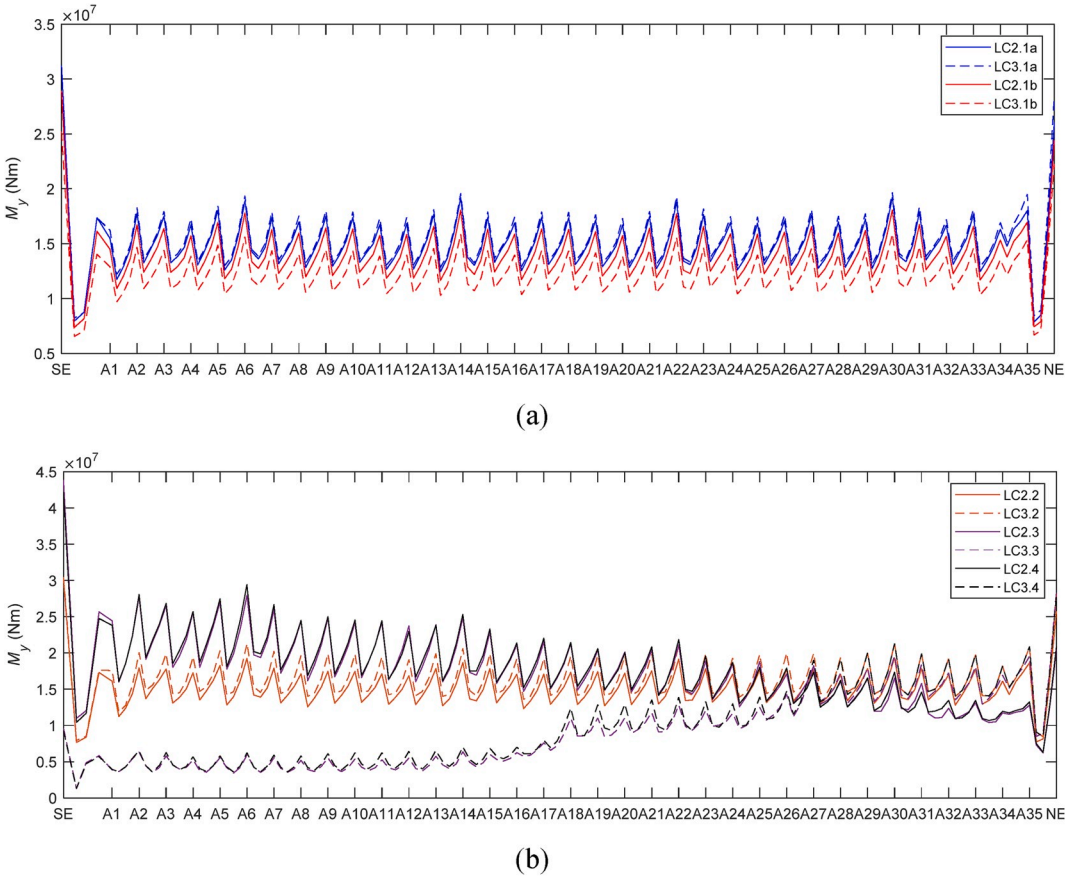

Fig. 21. Standard deviation of weak axis bending moment under 100-year wave load cases (LC2 and LC3): (a) homogeneous waves and (b) inhomogeneous waves.

onwards, wind waves at the Bjørnafjord are represented as short-crested with $n = 4$ [26].

Fig. 17 shows statistical values regarding the weak axis bending moment M_y along the entire length of the bridge girder. Similar to the results shown in Fig. 6 for 1-year wave load cases, the inhomogeneity in θ_p is found to be a key factor affecting the standard deviation of M_y. At girder location A27 where θ_p is identical for both homogeneous and inhomogeneous wave load cases, the induced dynamic weak axis bending moments are very close to each other. The discrepancy in the dynamic responses due to homogeneous and inhomogeneous wave load cases increases when moving away from A27. The effect of inhomogeneity in H_s is small as its spatial variation along the full length of the bridge is also small. In addition, M_y is found to be virtually unaffected by the coherence and correlation of waves at different pontoon locations. For the maximum and mean values of M_y, they are still governed by the static loads, i.e. self-weight of the bridge.

The statistical values of the bridge strong axis bending moment M_z are plotted in Fig. 18. As it can be seen, homogeneous wave load cases tend to result in higher maximum values and standard deviation of M_z than inhomogeneous wave load cases for the girder segment between the south end and A27. The discrepancies become small after A27. To reveal the cause of such differences, response spectrum analysis was carried out. As shown in Fig. 19, the strong axis bending moment responses excited by wave loads near the wave periods are similar for both homogeneous and inhomogeneous wave load cases. However, the excitation level is higher for the segment near the south end when the waves are homogeneous. Fig. 19 also shows that there is little response near the period of 30 s, which implies that the lowest transverse vibration modes give virtually no contribution to the strong axis bending moment along the girder.

As for the motions, they exhibit a similar trend to those observed for LC1. Note that 100-year wave conditions are often employed for ultimate limit state checks. Therefore, motion responses are of limited interest and not discussed in this paper.

4.4. 100-year wave load effects (LC3)

The study of LC1 and LC2 showed that the weak axis bending moment M_y and the vertical displacement u_z are most sensitive to inhomogeneous wave loads. They are significantly affected by the spatial variation of the principal wave direction θ_p. In LC3, θ_p is kept constant, but a large inhomogeneity in H_s and T_p is accounted for. Thus, the study on LC3 aims to reveal the effect of these wave properties on the bridge responses in an inhomogeneous wave condition. In addition, swell is included.

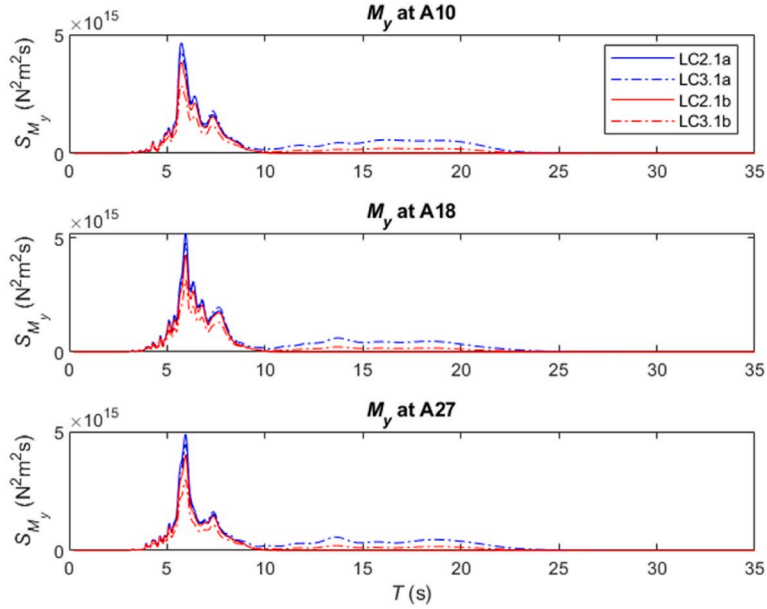

(a)

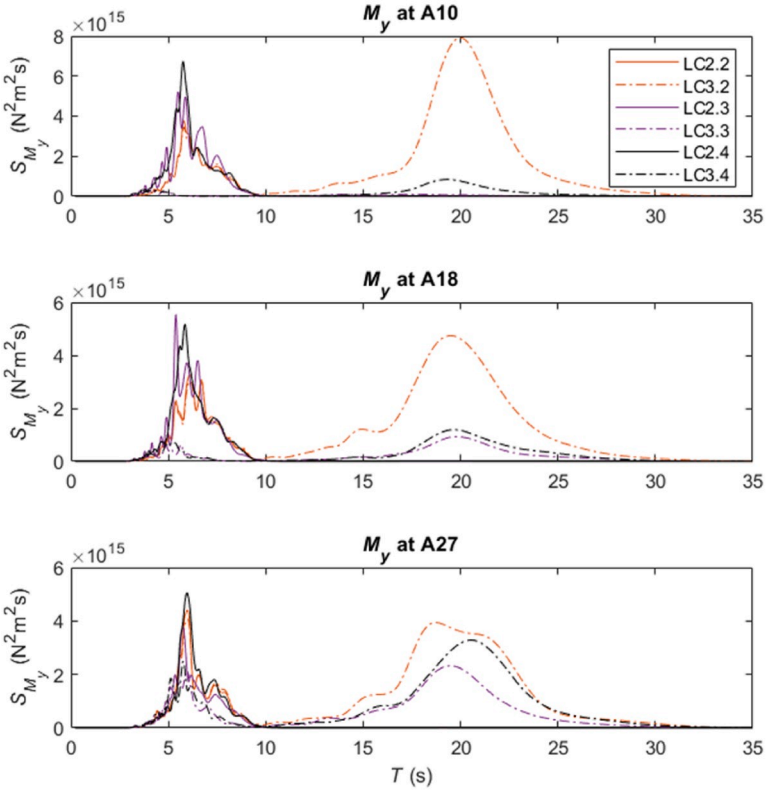

(b)

Fig. 22. Response spectra of weak axis bending moment under 100-year wave load cases (LC2 and LC3): (a) homogeneous waves and (b) inhomogeneous waves.

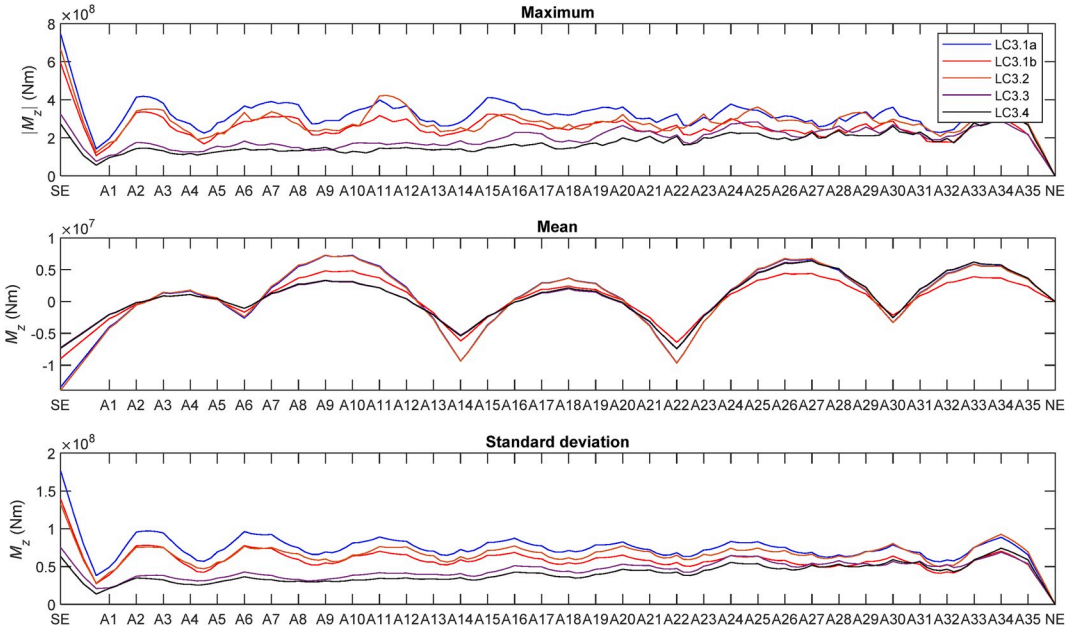

Fig. 23. Statistical values of strong axis bending moment under 100-year wave loads (LC3).

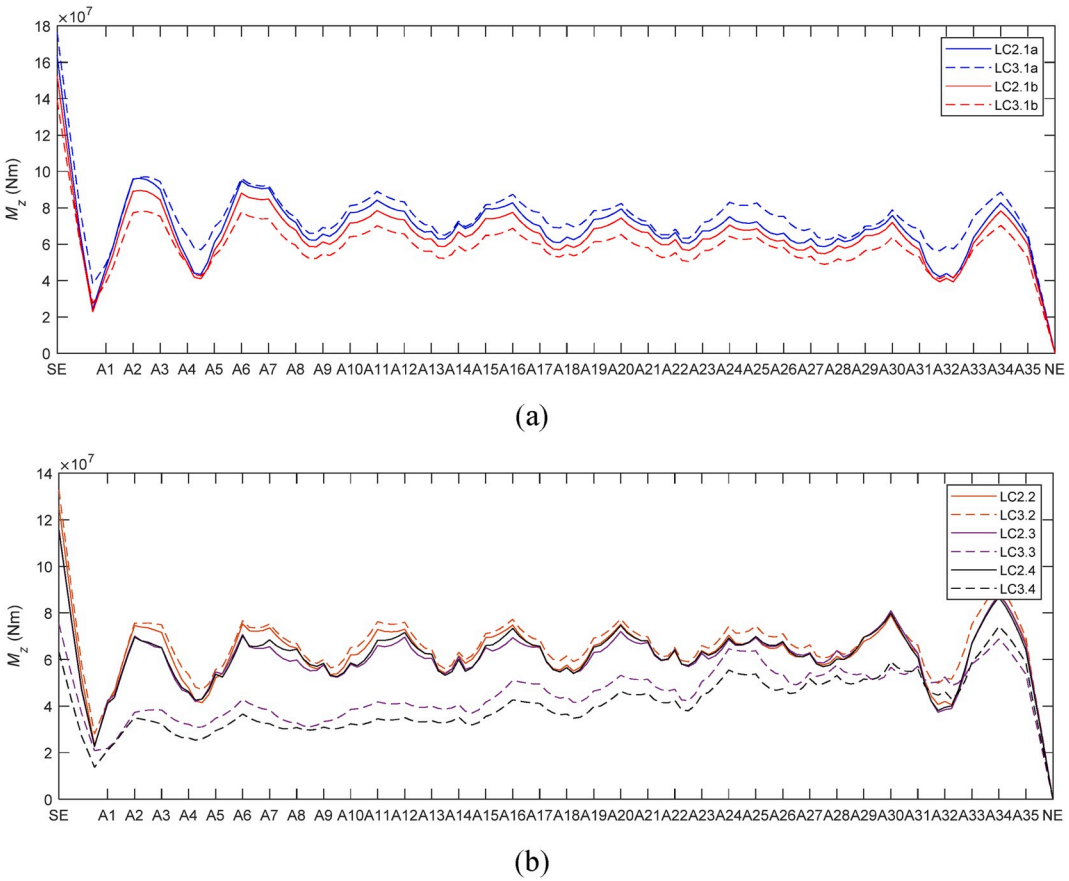

Fig. 24. Standard deviation of strong axis bending moment under 100-year wave load cases (LC2 and LC3): (a) homogeneous waves and (b) inhomogeneous waves.

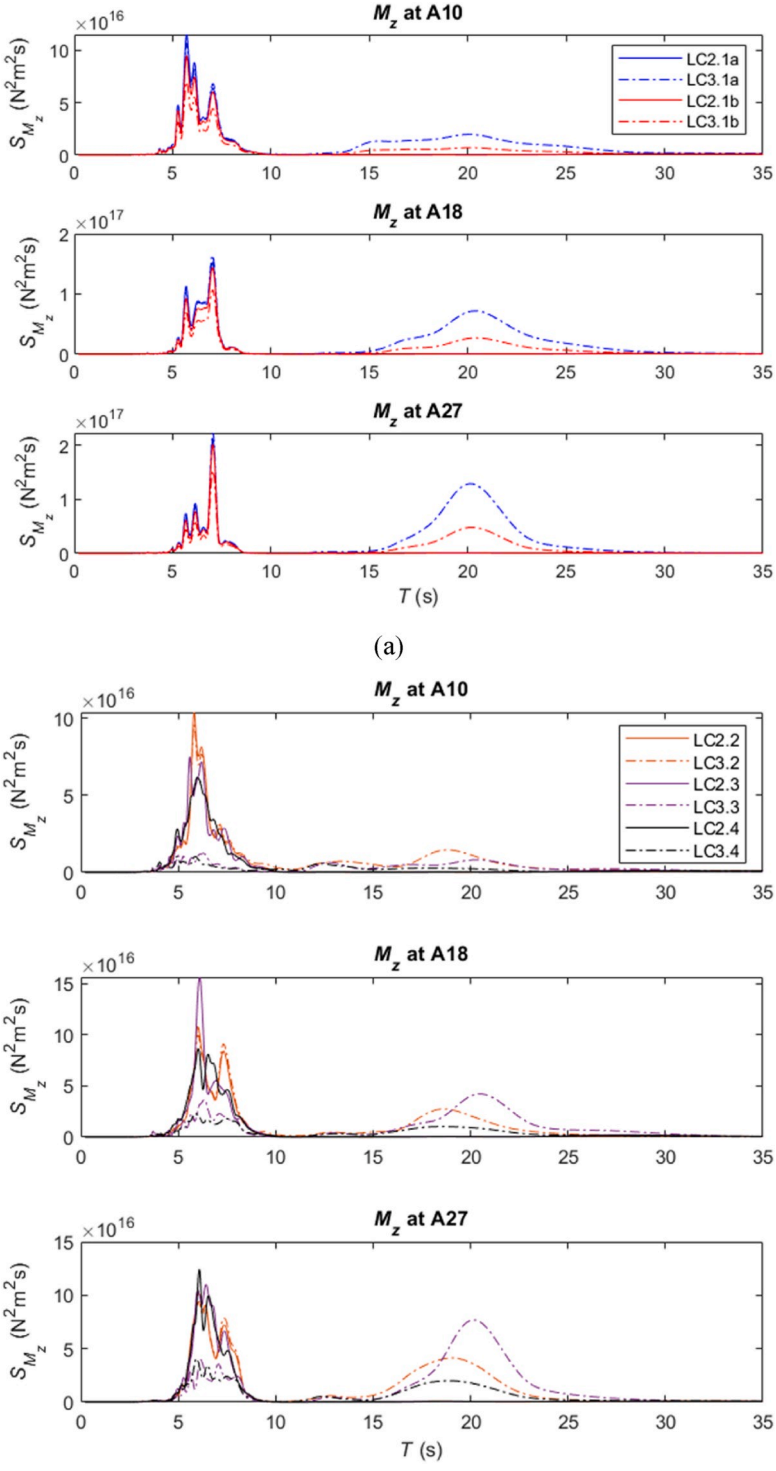

Fig. 25. Response spectra of strong axis bending moment under 100-year wave load cases (LC2 and LC3): (a) homogeneous waves and (b) inhomogeneous waves.

Fig. 20 shows the statistical values regarding the weak axis bending moment M_y of the bridge girder. As it can be seen, large variations in both H_s and T_p lead to significant differences in the standard deviation of M_y between homogeneous and inhomogeneous wave load cases, especially for the girder segment between the south end and A27. The lower responses for inhomogeneous wave load cases LC3.3 and LC3.4 may be attributed to the lower H_s and T_p of the waves. For the girder segment between A27 and the north end, H_s and T_p are identical for both homogeneous and inhomogeneous wave load cases. Consequently, the standard deviations of M_y are very similar.

Fig. 21 compares the standard deviation of M_y for LC2 and LC3. The comparison of homogeneous wave load cases shows that the results for LC2.1a and LC3.1a are very close to each other. This reveals that the inclusion of swell has a negligible effect on M_y. Response spectra of M_y plotted in Fig. 22(a) clearly show that the swell has a contribution to the M_y responses near the period of 20 s. However, due to the lack of vibration modes in the vicinity of that period (refer to Fig. 5), these responses are mainly forced vibrations without any resonant effects and thus their contribution to the dynamic M_y responses is limited. The comparison with inhomogeneous wave load cases (see Figs. 21(b) and 22(b)) shows that near the south end, more higher order vibration modes are excited by wind waves in LC3 than LC2 and the excitation level is lower. As it moves from A10 to A27, the increase in T_p results in a change from higher order modes to lower order modes being excited by the wind waves. In addition, an increase in the extent of excitation of modes by wind waves is also observed, due to the combined effect of increasing T_p and H_s. The swell also excited M_y responses near the period of 20 s. However, no resonance is expected and thus swell has a limited effect on the dynamic M_y responses.

Figs. 23 and 24 show the statistical values of the strong axis bending moment M_z of the bridge girder for LC3 and the comparison with LC2, respectively. As it can be seen, homogeneous wave load cases lead to larger M_z along the entire length of the bridge girder, even though the H_s and T_p are identical for both homogeneous and inhomogeneous wave load cases for the location between A27 and the north end. When compared with LC2, the standard deviations of M_z for inhomogeneous wave load cases (LC3.3 and LC3.4) are also smaller than those for LC2.3 and LC2.4 except for the girder segment near A32. The analysis of response spectra which are in Fig. 25 reveals that although both H_s and T_p increase as the location moves towards the bridge north end, the number of modes excited by the wind wave frequencies is still lower for LC3.3 and LC3.4 when compared with the LC2 load cases. It also reveals that the swell excited the strong axis bending moment responses especially for the segment near the north end. For homogeneous wave load cases, a significant increase of 39% in the standard deviation of M_z is observed at location A32 for LC3.1a when compared with LC2.1a. This also explains why for inhomogeneous load cases, the dynamic M_z responses appear larger for LC3 in the vicinity of A32. At other bridge locations, the effect of swell is found to be rather limited.

5. Conclusions

This paper presents a numerical study on the hydroelastic responses of a 4.6 km long straight and side-anchored floating pontoon bridge subjected to wave loads. The numerical model is based on the conceptual design of a floating bridge across the Bjørnafjord. The bridge is vertically supported by 35 evenly spaced pontoons. Four clusters of deep water mooring lines are engaged to limit the transverse response of the bridge. This study is based on an idealised bridge model. The comparison of the modal properties with the results from an independent study showed that the idealised bridge model can well capture the essential dynamic characteristics of the design concept.

In the study of inhomogeneous wave load effects on the bridge responses, inhomogeneities associated with the significant wave height H_s, wave peak period T_p, principal wave direction θ_p and coherence and correlation of waves at different locations are considered. The study employs two different types of wave inhomogeneity according to the wave conditions at the Bjørnafjord and the Sulafjord sites. The former characterises a relatively large spatial variation of θ_p while the latter presents abrupt changes in H_s and T_p. In general, the bridge responses exhibit a rather linear relationship with the spatial variation of H_s. The dynamic responses of the bridge relate directly to the wave periods. The effect of wave inhomogeneity is most significant on the vertical responses (M_y and u_z) as the natural periods of vertical vibration modes are close to the wave periods. Larger values of T_p in a wind sea are also found to give more excitation of the lower order bridge modes and thus the responses are larger. However, the inhomogeneous waves have a much smaller effect on the strong axis bending moment M_z of the bridge girder due to the lack of resonant responses. The wind-driven short-crested waves in a fjord also reduce the differences in the transverse responses induced by homogeneous and inhomogeneous waves when compared with unidirectional long-crested waves.

The inhomogeneity in θ_p is found to have a significant effect on the bridge responses. This is because oblique waves exert higher excitation forces to the pontoons when compared with beam sea conditions. As a result, the vertical responses of the bridge girder induced by inhomogeneous waves differ significantly from homogeneous waves when a large spatial variation of θ_p is present.

In all cases, the effects of coherence and correlation of waves at different locations in an inhomogeneous and short-crested wave condition are found to be small. This implies that the neglection of wave coherence and correlation in an inhomogeneous and short-crested wave condition in order to simplify the modelling and analysis for engineering design of the present type of floating bridge with a large number of pontoons may be acceptable.

Declaration of competing interest

The authors declare that they have no known competing financial interests or personal relationships that could have appeared to influence the work reported in this paper.

Acknowledgment

This work was supported by the Research Council of Norway through the project 268403/O80 Design and Verification of Large Floating Coastal Structures – Environmental description, structural loads, responses and mooring system.

References

[1] Brown J. Turning the tide of war: the Mulberry Harbors. Civ Eng 2013;83(12):46–9.
[2] Wikipedia. Hood canal bridge. Retrieved from: https://en.wikipedia.org/wiki/Hood_Canal_Bridge. [Accessed 16 September 2019].
[3] Kvåle KA, Sigbjörnsson R, Øiseth O. Modelling the stochastic dynamic behaviour of a pontoon bridge: a case study. Comput Struct 2016;165:123–35.
[4] Larssen RM, Jakobsen S. Submerged floating tunnels for crossing of wide and deep fjords. Proc Eng 2010;4:171–8.
[5] Maruyama T, Kawamura Y. Construction of a floating swing bridge – Yumemai bridge. Osaka Technol 2000;39:28–43.
[6] Holand I, Sigbjörnsson R, Langen I. Dynamic analysis of a curved floating bridge. In: IABSE proceedings; 1997. P-5/77.
[7] Langen I, Sigbjörnsson R. On stochastic dynamics of floating bridges. Eng Struct 1980;2(4):209–16.
[8] Langen I. Probabilistic methods for dynamic analysis of floating bridges. Norweg Marit Res 1983;11(1):2–15.
[9] Leira BJ. Probabilistic design – an application to floating bridges. SINTEF: Technical Report; 1983.
[10] Leira BJ, Langen I. On probabilistic design of a concrete floating bridge. Nord Concr Res 1984;3:140–66.
[11] Hartz B. Dynamic response of the hood-canal floating bridge. In: Second ASCE/EMD Specialty conference on dynamic response of structures. Atlanta, USA; 1981.
[12] Seif MS, Inoue Y. Dynamic analysis of floating bridges. Mar Struct 1998;11(1):29–46.
[13] Cheng Z, Svangstu E, Gao Z, Moan T. Field measurements of inhomogeneous wave conditions in Bjørnafjorden. J Waterw Port Coast Ocean Eng 2019;145(1):05018008.
[14] Fylling IJ. Dynamisk analyse av flytebrukonsept for Sulesund – Hareid. 2012. MARINTEK Report No. 580319.
[15] Cheng Z, Gao Z, Moan T. Hydrodynamic load modeling and analysis of a floating bridge in homogeneous wave conditions. Mar Struct 2018;59:122–41.
[16] Cheng Z, Gao Z, Moan T. Wave load effect analysis of a floating bridge in a fjord considering inhomogeneous wave conditions. Eng Struct 2018;163:197–214.
[17] Xiang X, Viuff T, Leira BJ, Øiseth O. Impact of hydrodynamic interaction between pontoons on global responses of a long floating bridge under wind waves. In: Proceedings of the 37th international conference on ocean, offshore and arctic engineering, Madrid, Spain, 17-22 June; 2018.
[18] Xiang X, Løken A. Hydroelastic analysis and validation of an end-anchored floating bridge under wave and current loads. In: Proceedings of the 38th international conference on ocean, offshore and arctic engineering, Glasgow, 9-14 June; 2019.
[19] Viuff T, Leira BJ, Xiang X, Øiseth O. Effects of wave directionality on extreme response for a long end-anchored floating bridge. Appl Ocean Res 2019;90:101843.
[20] Viuff T, Xiang X, Leira BJ, Øiseth O. Code-to-code verification of end-anchored floating bridge global analysis. In: Proceedings of the 37th international conference on ocean, offshore and arctic engineering, Madrid, Spain, 17-22 June; 2018.
[21] Sha Y, Amdahl J, Liu K. Design of steel bridge girders against ship forecastle collisions. Eng Struct 2019;196:109277.
[22] Sha Y, Amdahl. Numerical investigations of a prestressed pontoon wall subjected to ship collision loads. Ocean Eng 2019;172:234–44.
[23] Multiconsult. SBJ-31-C3-MUL-22-RE-100-0 – analysis and design (base case). Oslo, Norway: Multiconsult AS; 2017.
[24] DNV GL. SBJ-31-C3-DNV-62-RE-018-0 Bjørnafjorden side anchored floating bridge - independent global analyses. Oslo, Norway: DNV GL; 2018.
[25] Cummins WE. The impulse response function and ship motions. Washington DC: Report No. DTMB-1661; 1962.
[26] Vegvesen Statens. SBJ-32-C3-SVV-90-BA-002 Design basis Bjørnafjorden rev. Norway: E. Statens Vegvesen; 2018.
[27] Wei W, Fu S, Moan T, Lu Z, Deng S. A discrete-modules-based frequency domain hydroelasticity method for floating structures in inhomogeneous sea conditions. J Fluids Struct 2017;74:321–39.
[28] Wei W, Fu S, Moan T, Song C, Ren T. A time-domain method for hydroelasticity of very large floating structures in inhomogeneous sea conditions. Mar Struct 2018;57:180–92.
[29] Ding J, Tian C, Wu Y, Wang X, Liu X, Zhang K. A simplified method to estimate the hydroelastic responses of VLFS in the inhomogeneous waves. Ocean Eng 2019;172:434–45.
[30] WAMIT. WAMIT user manual version 7.3. USA: Chestnut Hill; 2019.
[31] SINTEF Ocean. RIFLEX 4.16.0 theory manual. Norway: Trondheim; 2019.
[32] SINTEF Ocean. SIMO 4.16.0 theory manual. Norway: Trondheim; 2019.
[33] Bathe KJ. Finite element procedures. New Jersey: Prentice Hall; 1996.
[34] Lie H, Fu S, Fylling I, Fredriksen AG, Bonnemaire B, Kjersem GL. Numerical modelling of floating and submerged bridges subjected to wave, current and wind. In: Proceedings of the 35th international conference on ocean, offshore and arctic engineering, Busan, 19-24 June; 2016.